



Geochemistry
Geophysics
Geosystems

G³

Article

Volume 12, Number

21 October 2011

Q0AC16, doi:10.1029/2011GC003834

ISSN: 1525-2027

Published by AGU and the Geochemical Society

The energetics of melting fertile heterogeneities within the depleted mantle

Richard F. Katz

*Department of Earth Sciences, University of Oxford, South Parks Road, Oxford OX1 3AN, UK
(richard.katz@earth.ox.ac.uk)*

John F. Rudge

Institute of Theoretical Geophysics, Bullard Laboratories, University of Cambridge, Madingley Road, Cambridge CB3 0EZ, UK (rudge@esc.cam.ac.uk)

[1] To explore the consequences of mantle heterogeneity for primary melt production, we develop a mathematical model of energy conservation for an upwelling, melting body of recycled oceanic crust embedded in the depleted upper mantle. We consider the end-member geometric cases of spherical blobs and tabular veins. The model predicts that thermal diffusion into the heterogeneity can cause a factor-of-two increase in the degree of melting for bodies with minimum dimension smaller than ~ 1 km, yielding melt fractions between 50 and 80%. The role of diffusion is quantified by an appropriately defined Peclet number, which represents the balance of diffusion-driven and adiabatic melting. At intermediate Peclet number, we show that melting a heterogeneity can cool the ambient mantle by up to ~ 20 K (spherical) or ~ 60 K (tabular) within a distance of two times the characteristic size of the body. At small Peclet number, where heterogeneities are expected to be in thermal equilibrium with the ambient mantle, we calculate the energetic effect of pyroxenite melting on the surrounding peridotite; we find that each 5% of recycled oceanic crust diminishes the peridotite degree of melting by 1–2%. Injection of the magma from highly molten bodies of recycled oceanic crust into a melting region of depleted upper mantle may nucleate reactive-dissolution channels that remain chemically isolated from the surrounding peridotite.

Components: 11,900 words, 9 figures, 1 table.

Keywords: eclogite; heat conduction; magma; mantle heterogeneity; partial melting; pyroxenite.

Index Terms: 1011 Geochemistry: Thermodynamics (0766, 3611, 8411); 1037 Geochemistry: Magma genesis and partial melting (3619); 5134 Physical Properties of Rocks: Thermal properties.

Received 12 August 2011; **Revised** 16 September 2011; **Accepted** 18 September 2011; **Published** 21 October 2011.

Katz, R. F., and J. F. Rudge (2011), The energetics of melting fertile heterogeneities within the depleted mantle, *Geochem. Geophys. Geosyst.*, 12, Q0AC16, doi:10.1029/2011GC003834.

Theme: Geochemical Heterogeneities in Oceanic Island Basalt and Mid-ocean Ridge
Basalt Sources: Implications For Melting Processes and Mantle Dynamics

Guest Editors: C. Beier and P. Asimow

1. Introduction

[2] It is well established that the mantle is chemically heterogeneous on length-scales smaller than the 100 km typical size of the melting region beneath a plate-boundary or hot spot volcano [e.g., Hofmann, 1997]. Despite this, most studies of melting at plate tectonic boundaries and hot spots still treat the mantle as a homogeneous source. Such models, irrespective of their sophistication, probably miss crucial aspects of basalt petrogenesis; they may therefore lead to incorrect inversions of geochemical data for mantle properties and processes. Treatment of melting of a lithologically heterogeneous mantle remains largely qualitative, lacking the rigor necessary for quantitative geochemical modeling. The present work seeks to address this deficiency.

[3] A range of studies have inferred that heterogeneities are formed from previously subducted oceanic and continental crust and lithosphere [e.g., Hofmann and White, 1982; Willbold and Stracke, 2010] that has been stirred into the mantle over geologic time. This stirring continuously reduces the characteristic size of heterogeneities [Hoffman and McKenzie, 1985; Allègre and Turcotte, 1986], and increases the rate of homogenization by solid-state diffusion. The surviving heterogeneities are those that remain larger than the decimeter scale over which diffusion would erase chemical variations on the billion-year time-scale of mantle convection [Hofmann and Hart, 1978]. Many of these have a pyroxene-rich lithology that may contain garnet, spinel, and other accessory phases, but has little or no olivine. In this paper, we do not attempt to distinguish between the pyroxenites, garnet pyroxenites, and eclogites that are included in this range of lithologies; rather we generalize them to a class of mantle heterogeneity composed of fertile, recycled crustal rocks. We do not directly address other classes of mantle heterogeneity such as recycled sediments.

[4] Within the class considered here, the size-distribution and concentration of heterogeneities throughout the mantle remains the subject of controversy. Geochemical measurements and models put constraints on the proportion of enriched materials in the source regions of mid-ocean ridges. Hirschmann and Stolper [1996] used a variety of trace element and isotopic measurements to estimate that the MORB-source contains 3–6% garnet pyroxenite. Melting experiments by Pertermann and Hirschmann [2003a] more accurately determined the productivity of upwelling pyroxenite,

and lead them to suggest 2–3% pyroxenite, though they note that this result is sensitive to the assumed fertility of the pyroxenite. Sobolev *et al.* [2007] studied trace element and forsterite content in olivine phenocrysts from MORB, OIB, komatiites, and within-plate lavas and suggested that variations in Mn and Ni content, among other indicators, call for about 5% recycled oceanic crust in the MORB source and 20% in the OIB source. This is approximately consistent with estimates by Ito and Mahoney [2005], determined by modeling the melting process for ridges and plumes, and seeking the range of starting compositions that can explain both OIB and MORB geochemical and isotopic systematics. Each of these studies used a different approach to quantify the contribution of recycled oceanic crust, yet their results are similar; it seems reasonable to expect that enriched heterogeneities compose less than one fifth of the mantle that melts at most ridges and hot spots.

[5] Constraining the sizes and shapes of mantle heterogeneities has proven more difficult than determining their relative proportion. Seismic scattering techniques described by Helffrich [2006] provide support for blobs of mineralogically distinct heterogeneities with a characteristic scale of ≈ 10 km, distributed uniformly throughout the mantle. Kogiso *et al.* [2004] argued for a size of ≈ 1 m, which they calculated based on the observational constraint of radiogenic osmium signatures in rocks recovered from mid-ocean ridges and hot spots. Yasuda and Fujii [1998] noted that the negative buoyancy of eclogite blobs means that blobs of diameter 40 km or larger cannot ascend through the upper mantle, though the density that they assumed for eclogite may have been too large [Pertermann and Hirschmann, 2003b]. Others have argued for heterogeneity of equal magnitude at all scales based on observed geographical variation in the isotopic ratios of lavas [e.g., Gurnis, 1986].

[6] Since fertile heterogeneities are a small fraction of mantle volume, and are apparently dispersed at sizes smaller than 10 km, we study their melting systematics using an idealized model of an isolated heterogeneity. Such a heterogeneity would initially be in thermal equilibrium with the surrounding mantle, because the rate of thermal diffusion is fast relative to that of convective overturning. Because of its composition, it would begin decompression melting at higher pressures than the ambient, more depleted mantle. This melting requires energy to convert solid to liquid, and it diminishes the temperature of the blob relative to the surrounding mantle. The associated temperature gradient drives heat flow into the blob, and increases the melting



rate, while cooling the surrounding mantle. What is the magnitude of this effect? This question was first addressed by *Sleep* [1984], who developed models of heat conduction into a fertile, melting sphere and tabular body.

[7] *Sleep* [1984] considered a fertile heterogeneity undergoing decompression melting at an upwelling rate of 3 cm/yr and calculated the size it must have such that the characteristic thermal-diffusion time is approximately equal to its duration in the melting column, obtaining a value of 5 km. Moreover, he recognized that heterogeneities much smaller than this size would melt in thermal equilibrium with the surrounding mantle, while those much larger would melt in thermal isolation. *Sleep* [1984] then derived a mathematical model of partial melting of such heterogeneities based on diffusive heat flow and parameterized thermodynamic properties. Analysis of this model lead him to conclude that thermal diffusion could cause an enhancement of melting by up to a factor of seven over the thermally isolated case. This extremely large enhancement contrasts with the results that we present below.

[8] In the present paper we take a similar approach to *Sleep* [1984]—we consider thermal diffusion into a fertile heterogeneity of spherical or tabular shape—but we provide a more comprehensive study and obtain significantly different results. Our approach is more rigorous in that we derive an equation for conservation of energy that explicitly couples melting with thermal diffusion. In contrast to *Sleep* [1984], we obtain full analytical solutions in terms of non-dimensional parameters, and use them to elucidate the controls on and limits of partial melting of heterogeneities. Furthermore, on empirical [*Pertermann and Hirschmann, 2003a*] and theoretical grounds [*Hirschmann et al., 1999*], we consider the nonlinear relationship between melt fraction and temperature, where *Sleep* [1984] assumed linearity. For the nonlinear case, we rely on numerical solutions of the governing equations; these are documented and validated in Appendix B. Our calculations are based on parameter values from published experiments on G2 pyroxenite [*Pertermann and Hirschmann, 2003a*], which has a composition thought to approximate recycled oceanic crust. We compare the results of these calculations with those obtained by *Sleep* [1984], who used different and probably unrealistic parameters for pyroxenite melting (for example, *Sleep* [1984] assumed a near-solidus isobaric productivity $\partial F/\partial T|_P$ that is a factor of five to twenty times larger than the value obtained empirically by *Pertermann and Hirschmann* [2003a]).

[9] Our work is also related to that of *Phipps Morgan* [2001], who considered narrow, multilayered tabular veins of fertile pyroxenite within depleted peridotite, and computed melting behavior for a variety of compositional scenarios. He assumed thermal equilibrium between all the layers in the model. Similar models were developed by *Hirschmann and Stolper* [1996] and *Stolper and Asimow* [2007]. And whereas these authors' work focused on the effects of melting a compositional mélange with variable solidus (and solidus slope) between solid phases, here we are interested in accounting for the finite time-scale of thermal equilibration. Our model is not restricted to any one set of pyroxenite melting parameters, though in this paper we limit consideration to a single example that we hope is representative.

[10] The relative simplicity of the physical model is based on a number of key assumptions. The most important of these is that heterogeneities are isolated from one another, such that their thermal disturbances do not interact. We further assume that the characteristic size of a heterogeneity is small relative to the vertical distance between the depth at which it reaches its solidus and the depth of the ambient mantle solidus. This latter assumption allows us to approximate the lithostatic pressure as being constant within the heterogeneity. We assume that heterogeneities upwell at the same speed as the ambient mantle; other authors have considered the possibility that chemically dense, unmolten, recycled material upwells at a slower speed due to its negative buoyancy [*Yasuda and Fujii, 1998; Pertermann and Hirschmann, 2003b*]. Finally, we assume that melt does not segregate from the host rock, which is the thermodynamic equivalent of assuming batch melting. If the ambient mantle remains unmolten as an embedded heterogeneity partially melts, magma may be held within the heterogeneity by a permeability barrier. Alternatively, it may chemically react with the surrounding rock [*Yaxley and Green, 1998; Kogiso et al., 2004*], propagate through it by diking, or open the pores through surface-energy driven flow [*Riley and Kohlstedt, 1991*]. Even a leaky permeability barrier around a fertile enclave would significantly restrict magmatic segregation if the scale of the sphere is smaller than the compaction length [*Spiegelman, 1993*]. For the case of a tabular vein, these arguments are clearly tenuous; we therefore justify the assumption on grounds of mathematical convenience, and flag this as an issue to be remedied in future work. These assumptions enable us to formulate a mathematical model that admits analytical

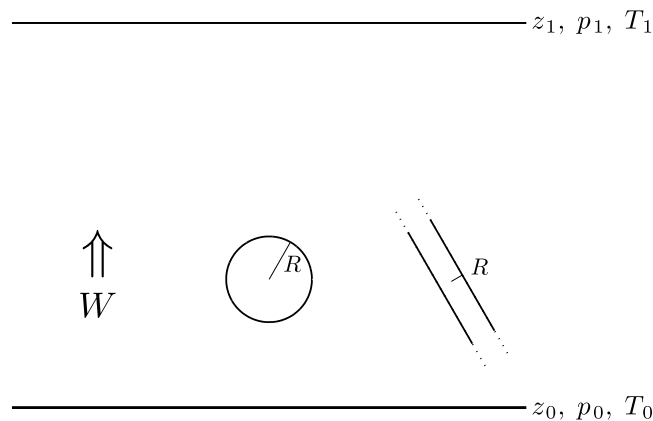


Figure 1. Schematic diagram of the upwelling column with idealized fertile blob and fertile tabular vein. The blob is a sphere in three dimensions, while the tabular vein is an infinite sheet. The fertile material crosses its solidus at $z = z_0$ and $t = 0$; far-field ambient mantle crosses its solidus at $z = z_1$ and $t = t_1$.

solution in some cases, and high-accuracy, efficient numerical solutions in others. We can thus provide a thorough exploration of the model behavior, and draw conclusions that will inform more detailed work in which assumptions are relaxed.

[11] Although this paper focuses on the energetics of pyroxenite melting, the results also have geochemical implications. It is well-known that garnet is an important phase in recycled oceanic crust, and that it has a unique set of affinities for trace elements [e.g., *Stracke et al.*, 1999; *Pertermann et al.*, 2004]. The trace element budget of melts derived from pyroxenite is therefore sensitive to the presence of residual garnet; the persistence of garnet in the residue depends on pressure, but it also depends on the degree of melting. The work presented here provides a framework for evaluating the degree of melting of pyroxenite enclaves within the depleted, peridotite upper mantle; it also highlights the difficulties in inverting geochemical data for the physical characteristics of mantle heterogeneity by showing that the size and shape of heterogeneities has a significant influence on their melting behavior. Perhaps a larger difficulty is that the pathways of melt transport from deep-melting, fertile heterogeneities to the surface are poorly constrained, and it is increasingly understood that the details of melt transport have a crucial impact on observed geochemical patterns [e.g., *Spiegelman and Kelemen*, 2003; *Liang et al.*, 2011].

[12] The next section describes the idealized physical scenario to be analyzed, and lays out a mathematical formulation of the problem. The Results section then presents non-dimensional output from analytical and numerical solutions. The Discussion section examines these results in more

detail and provides a subset of them in dimensional form. We summarize our findings briefly at the end, and give the details of analytical and numerical methods in two appendices. Throughout this paper, the focus is on the slightly more complicated case of a spherical heterogeneity, however in the Discussion section, we compare our results for spherical and tabular bodies.

2. The Mathematical Model

[13] Figure 1 is a schematic representation of the model set-up. We consider two end-member cases: a spherical blob of radius R and an infinite tabular vein of half-width R . Both are made of a uniform, fertile lithology, and are embedded within the depleted upper mantle, upwelling at speed $W > 0$. We develop the mathematical model using the case of the spherical blob and present the case of a tabular vein in Section 2.3.

[14] We assume that the blob is small enough that we can neglect vertical variation of all properties within it. This assumption is awkward for the tabular vein, but not unreasonable if we consider that temperature gradients (and hence heat flow) normal to the vein will greatly exceed those within it. As the heterogeneity ascends, it reaches a pressure $p_0 = \rho g z_0$ where its temperature is equal to the solidus temperature T_0 ; we label this moment $t = 0$ (ρ is the density of all materials under consideration; g is the acceleration due to gravity; both are assumed constant). The ambient mantle is also upwelling with speed W , and it reaches its solidus temperature T_1 at a shallower pressure $p_1 = \rho g z_1$ (and hence at a later time $t = t_1$). We investigate the time interval between 0 and t_1 , when the blob is

Table 1. Dimensional and Non-Dimensional Parameters

Parameter	Value or Range	Units	Comment
a	0.25 – 1	-	Coefficient in melting relation (11)
c_p	1200	J kg ⁻¹ K ⁻¹	Specific heat capacity
g	10	m s ⁻²	Gravitational acceleration
k	= $\rho c_p \kappa$	J K ⁻¹ m ⁻¹ s ⁻¹	Thermal conductivity
L	4×10^5	J kg ⁻¹	Latent heat of melting
R	$10^{-2} - 10^3$	km	Characteristic size of heterogeneity
T_0	1623	K	Reference melting temperature
W	$10^{-1} - 10^3$	cm a ⁻¹	Upwelling rate
α	3×10^{-5}	K ⁻¹	Thermal expansivity
γ	8.3×10^6	Pa K ⁻¹	Clausius-Clapeyron slope (120 K/GPa)
Δp	1.7×10^9	Pa	Pressure interval (110–60 km depth)
ΔT	250	K	T -difference between liquidus and solidus
κ	10^{-6}	m ² s ⁻¹	Thermal diffusivity
ρ	3300	kg m ⁻³	Density
\mathcal{A}	0.1	-	Adiabatic parameter
$\Delta\theta$	1.2	-	Melting-temperature interval
Pe	-	-	Peclet number
S	1.7	-	Stefan number

partially molten but the ambient mantle is entirely solid.

[15] Motivated by the experimental results of *Pertermann and Hirschmann* [2003a], the solidus and liquidus temperatures of the blob are taken to depend on pressure only:

$$T_s(p) = T_0 + \gamma^{-1}(p - p_0), \quad (1a)$$

$$T_l(p) = T_0 + \gamma^{-1}(p - p_0) + \Delta T, \quad (1b)$$

where ΔT is a constant and γ is the Clapeyron slope. Because of the uniform upward motion, the pressure experienced by the blob changes with time according to

$$p(t) = p_0 - \rho g W t. \quad (2)$$

[16] The coordinate system is fixed to the center of the spherical heterogeneity, which has a radius R . The goal is to determine the temperature field $T(r, t)$ outside the blob as it melts, and to calculate the average temperature and melting rate within the blob. Magmatic segregation can be neglected if the blob is much smaller than the compaction length within it. This will be true for smaller values of R , but since we are concerned only with the averaged melting properties of the blob, we expect that mass redistribution within the blob would have only a small effect on our results.

[17] With the above assumptions, conservation of energy is

$$\frac{\partial H}{\partial t} + \rho g W = k \nabla^2 T, \quad (3)$$

where $\rho g W$ is the rate of change of potential energy and

$$dH = \rho L dF + \rho c_p dT + (1 - \alpha T) dp \quad (4)$$

represents an infinitesimal change in bulk enthalpy in terms of its contributing parts. F here is the volume fraction of melt, and the remaining symbols are defined in Table 1. Combining (2), (3), and (4) gives

$$\rho L \frac{\partial F}{\partial t} + \rho c_p \frac{\partial T}{\partial t} - \alpha T \frac{\partial p}{\partial t} = k \nabla^2 T. \quad (5)$$

[18] We will non-dimensionalize with the following scales

$$[x] = R, \quad [t] = \frac{\Delta p}{\rho g W}, \quad (6)$$

and define the non-dimensional temperature and pressure as

$$\theta = \frac{\gamma}{\Delta p} (T - T_0), \quad P = \frac{p - p_0}{\Delta p}, \quad (7)$$

where $\Delta p = p_0 - p_1$ and the temperature scale is the change in the solidus temperature from p_0 to p_1 . Using these scales and linearizing the adiabatic gradient about $T = T_0$ gives

$$S \frac{\partial F}{\partial t} + \frac{\partial \theta}{\partial t} + \mathcal{A} = \frac{1}{\text{Pe}} \nabla^2 \theta, \quad (8)$$

where the Peclet number is

$$\text{Pe} = \frac{\tau_R}{\tau_a} = \frac{\rho g W R^2}{\kappa \Delta p},$$

the Stefan number is

$$S = \frac{L\gamma}{c_p \Delta p},$$

and the adiabatic parameter is

$$A = \frac{\alpha \gamma T_0}{\rho c_p}.$$

All symbols in equation (8) represent non-dimensional quantities. The Peclet number is the ratio of the time-scale $\tau_R = R^2/\kappa$ for diffusion of heat across the blob to the time-scale $\tau_a = \Delta p/(\rho g W)$ for advection of the blob from p_0 to p_1 . It is the principal control parameter in the problem; for $Pe \rightarrow 0$ the diffusive heat transport dominates the thermal budget and the blob is in thermal equilibrium with the surrounding mantle, while for $Pe \rightarrow \infty$, diffusion is negligible relative to advective transport, and the blob melts adiabatically.

[19] The adiabatic parameter is the linearized rate of energy consumption by adiabatic expansion. We neglect the term associated with the adiabatic parameter in what follows. In A5 we show that incorporating this term gives rise to the usual adiabatic temperature gradient, and introduces a factor of $(1 - A)$ into the melt productivity.

[20] With the above scaling, the equations for the solidus and liquidus (1) become

$$\theta_s = P = -t, \quad (9a)$$

$$\theta_l = P + \Delta\theta = -t + \Delta\theta, \quad (9b)$$

where $\Delta\theta = \gamma \Delta T / \Delta p$ is the non-dimensional, constant temperature offset between solidus and liquidus. The non-dimensional pressure is given by $P(t) = -t$ with $0 \leq t \leq 1$.

[21] We can put rough constraints on all of the material parameters, as given in Table 1, but cannot prescribe the radius of the blob or its upwelling rate. However, these latter two parameters are combined in the Peclet number, so we need explore the variation in only a single dimensionless parameter. Note that a value of $\Delta\theta$ larger than unity indicates that the temperature difference between the solidus and the liquidus of the blob is larger than the temperature difference between its solidus for non-dimensional pressures $P = 0$ and $P = -1$. This means that for $\Delta\theta > 1$ and $t \leq 1$, the blob *cannot* melt to $F = 1$. In the current work we do not consider the case of a fully molten heterogeneity, which can only occur for $t \leq 1$ if $\Delta\theta \leq 1$.

2.1. Within the Blob

[22] Since we are interested in melting of a fertile blob of recycled material, we first formulate equations that capture its melting properties.

2.1.1. Simplified Melting Relations for Fertile, Recycled Oceanic Crust

[23] When the temperature within the blob is above the solidus, a dimensionless normalized temperature is

$$\Theta = \frac{\theta - \theta_s}{\Delta\theta}, \quad \text{when } \theta_s \leq \theta \leq \theta_l. \quad (10)$$

[24] *Pertermann and Hirschmann* [2003a] found, for the anhydrous pyroxenite composition G2 (N.B. *Pertermann and Hirschmann* [2003a] use the term pyroxenite to describe all pyroxene-rich, olivine-poor mantle heterogeneities), that the relationship between the non-dimensional normalized temperature Θ and the degree of melting can be represented as

$$F = a\Theta + (1 - a)\Theta^2, \quad (11)$$

where $0 \leq a \leq 1$. Their data was best fit for $a \approx 1/4$. Their pyroxenite composition, chosen to be similar to typical oceanic crust, cannot represent *all* flavors of mantle heterogeneity. It is, instead, a well-characterized and important example. We assert that the melting consequences of other compositions can be investigated within the mathematical framework established below, by repeating our calculations with modified values for material constants. For example, one could model the presence of volatile elements in the pyroxenite by modifying parameters T_0 , p_0 and a to produce a ‘‘tail’’ of low- F melting at high pressure [*Hirschmann et al.*, 1999].

2.1.2. The Degree of Melting of the Blob

[25] To simplify the analysis, we now assume a homogeneous distribution of temperature and melt fraction within the blob, and define these as θ_B and F_B respectively. This approximation will hold at small Peclet numbers; in Section 3.3 we relax this constraint and consider radially variable blobs. Proceeding with the averaged quantities θ_B and F_B , we can integrate equation (8) over the non-dimensional volume of the blob $V = 4\pi/3$. This gives

$$S \frac{\partial F_B}{\partial t} + \frac{\partial \theta_B}{\partial t} = \frac{3}{4\pi} \frac{1}{Pe} \int_S \nabla \theta \cdot \mathbf{dS}, \quad (12)$$

where we have used the divergence theorem to convert the volume integral into a surface integral. We can evaluate this integral in spherical coordinates as the spherically symmetric gradient in the radial direction times the non-dimensional surface area of the blob 4π . We then integrate with respect to time to obtain

$$SF_B + \theta_B = \frac{3}{\text{Pe}} \int_0^t \left. \frac{\partial \theta}{\partial r} \right|_{1,\tau} d\tau. \quad (13)$$

[26] Both θ_B and F_B can be expressed in terms of Θ_B by using (10) and (11). Equation (13) becomes

$$(\Delta\theta + aS)\Theta_B + (1-a)S\Theta_B^2 = t + \frac{3}{\text{Pe}} \int_0^t \left. \frac{\partial \theta}{\partial r} \right|_{1,\tau} d\tau, \quad (14)$$

which relates the homologous temperature inside the blob to the integrated heat flux into the blob from the ambient mantle. The above equation can be solved for Θ_B ; the result is

$$\Theta_B = \frac{\sqrt{1 + 4\Lambda f_B} - 1}{2\Lambda}, \quad (15)$$

where

$$\Lambda = \frac{(1-a)S}{\Delta\theta + aS}, \quad f_B = \frac{1}{aS + \Delta\theta} \left(t + \frac{3}{\text{Pe}} \int_0^t \left. \frac{\partial \theta}{\partial r} \right|_{1,\tau} d\tau \right). \quad (16)$$

In the linear limit where $a \rightarrow 1$ ($\Lambda \rightarrow 0$), equations (15) and (16) simplify to

$$\Theta_B = f_B = \frac{1}{S + \Delta\theta} \left(t + \frac{3}{\text{Pe}} \int_0^t \left. \frac{\partial \theta}{\partial r} \right|_{1,\tau} d\tau \right). \quad (17)$$

This linear case can be treated analytically; details are provided in A.

2.2. Outside the Blob

[27] Outside the blob, the mantle is below its solidus and hence $F = 0$. Equation (8) becomes

$$\frac{\partial \theta}{\partial t} = \frac{1}{\text{Pe}} \frac{1}{r^2} \frac{\partial}{\partial r} \left(r^2 \frac{\partial \theta}{\partial r} \right), \quad (18)$$

where we have chosen spherical coordinates and used the symmetry of the problem to discard terms.

[28] Equation (18) has boundary conditions

$$\theta(1, t) = -t + \Theta_B \Delta\theta, \quad (19a)$$

$$\theta(\infty, t) = 0, \quad (19b)$$

where Θ_B is given by (15) and (16). The first of these boundary conditions represents the continuity

of temperature at the surface of the blob, and the second represents the constant far-field temperature of the ambient mantle. The initial condition is uniform temperature,

$$\theta(r, 0) = 0. \quad (20)$$

2.3. A Tabular Heterogeneity

[29] The governing equations are simplified slightly if we consider a tabular heterogeneity of half-width R and infinite extent; equations (14) and (18) are replaced by

$$(\Delta\theta + aS)\Theta_B + (1-a)S\Theta_B^2 = t + \frac{1}{\text{Pe}} \int_0^t \left. \frac{\partial \theta}{\partial x} \right|_{1,\tau} d\tau, \quad (21)$$

$$\frac{\partial \theta}{\partial t} = \frac{1}{\text{Pe}} \frac{\partial^2 \theta}{\partial x^2}, \quad (22)$$

where we have taken the x -axis in the direction normal to the tabular body. The boundary conditions (19) are unchanged, except for use of the modified solution for Θ_B . As with the spherical blob, we neglect magmatic segregation for the tabular body. A model similar to this was considered by *Sleep* [1984]. In the Results section, we limit our attention to solutions for the spherical blob. The tabular vein is reintroduced in the Discussion section, where we examine the consequences of blob shape on melting behavior, for these two end-member cases.

[30] For a spherical (or tabular) blob, the solution is obtained by solving the system of equations (14) and (18) (or (21) and (22)), with (16), (19), and (20) on the domain $1 \leq (r, x) < \infty$ and $0 \leq t \leq 1$ for given values of a , Pe , S , and $\Delta\theta$.

[31] In the end-member cases of melting for infinite and zero Peclet number corresponding, respectively, to purely adiabatic and purely isothermal melting, it is not necessary to solve for the temperature structure outside the blob [*Sleep*, 1984]. Figure 2 shows a schematic representation of the temperature–pressure path taken by the blob in these two cases, and illustrates the thermodynamic phase diagram (for $a = 1$). Solutions for intermediate Peclet numbers follow paths between the end-member curves, but must be obtained through analytical or numerical solutions to the governing equations. These are presented in the next section.

3. Results

[32] In this section we present results from both analytical and numerical solutions of the governing

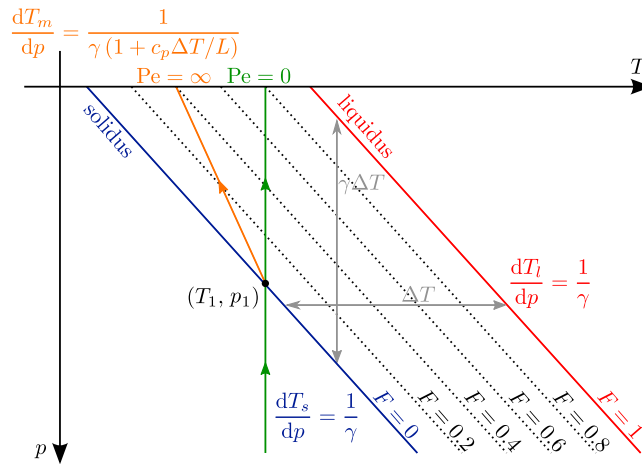


Figure 2. Thermodynamic analysis of the melting of the blob in the two extreme cases of complete thermal isolation ($Pe = \infty$) and complete thermal equilibration ($Pe = 0$). Diagram based on *Sleep* [1984, Figure 5]. Orange and green lines represent temperature–pressure paths for these extremes. Linear solidus and liquidus lines are assumed (red and blue lines), the dependence of melt fraction on homologous temperature is taken to be linear (i.e., $a = 1$), and we neglect the adiabatic temperature gradient (i.e., $\mathcal{A} = 0$). Degrees of melting are depicted by dotted contours.

equations for a spherical blob. We fix all the dimensionless parameters except the Peclet number, which captures the variation in both upwelling rate and blob size. Solutions are presented for a range of Peclet numbers.

3.1. Linear Melting Approximation

[33] When $a = 1$, the boundary condition described by (17) and (19a) is linear and an analytical solution can be obtained using Laplace transforms (see section A1). These are plotted in Figure 3 for different values of the Peclet number. Figure 3a shows

the degree of melting of the blob as a function of time. The range of curves is bounded by dashed lines for solutions at asymptotic values of Pe . When $Pe \rightarrow 0$, the blob is in thermal equilibrium with its surroundings. In this case, the degree of melting is determined entirely by the Clapeyron slope and the relationship between temperature and degree of melting in (11). Blobs of radius $\mathcal{O}(1$ km) or smaller would behave according to the small-Peclet limit. When $Pe \rightarrow \infty$, the blob is a closed thermodynamic system, exchanging no heat with the surrounding mantle. In this case, the degree of melting is controlled by the decreasing solidus

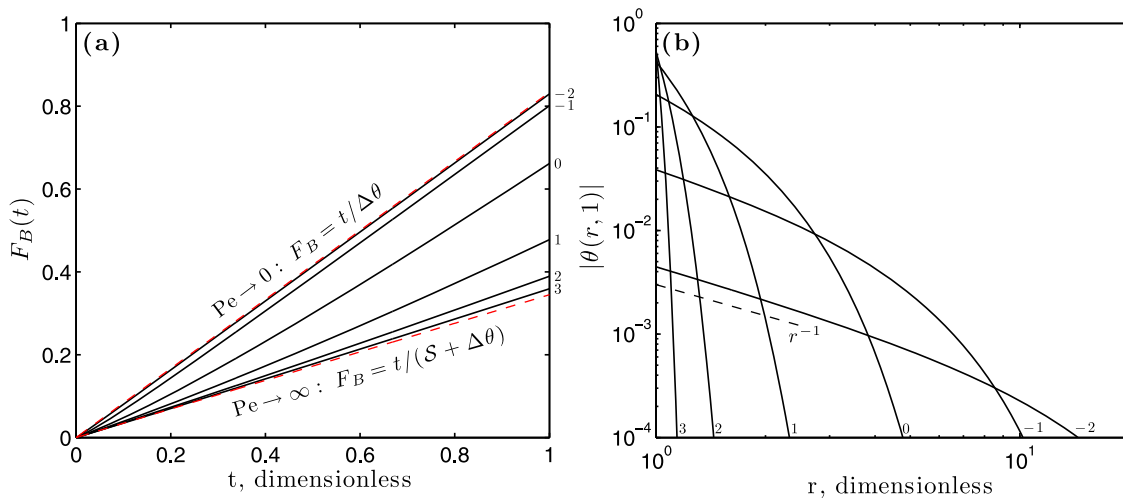


Figure 3. Analytical solution for equations (17)–(20) with $a = 1$ and other parameters as in Table 1. Curves are labeled with $\log_{10} Pe$. (a) The mean degree of melting within the blob as a function of time, for different values of Pe . The red dashed curves are the limiting cases of $Pe \rightarrow 0$ and $Pe \rightarrow \infty$. (b) The dimensionless temperature disturbance $|\theta(r, 1)|$ caused by diffusion into the blob as a function of dimensionless radius at the dimensionless time $t = 1$.

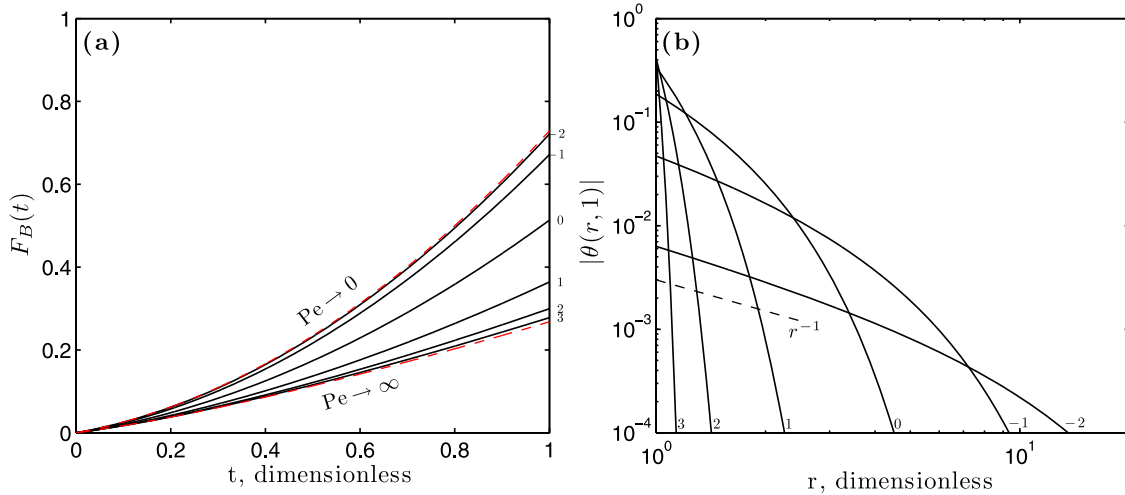


Figure 4. Numerical solutions for equations (15), (16), and (18)–(20) with $a = 1/4$ and other parameters as in Table 1. Each curve is labeled with $\log_{10} \text{Pe}$. Details as in Figure 3.

temperature and the latent-heat cost of melting. Blobs of radius $\mathcal{O}(100 \text{ km})$ or larger would behave according to the large-Peclet limit. Further dimensional considerations are deferred to the discussion section, below.

[34] For finite values of Pe , the ambient thermal state, $\theta(r, 0) = 0$, is altered by diffusion of heat into the relatively cool blob. The magnitude of the disturbance is plotted in Figure 3b for $t = 1$. The amplitude of the near-field disturbance grows with increasing Pe , while the decay length of the disturbance decreases. In other words, when diffusion is unimportant ($\text{Pe} \rightarrow \infty$), temperature differences from the background are large, but the radius of the thermal halo is small. When diffusion is important ($\text{Pe} \rightarrow 0$), the opposite is true. In the latter case, where diffusive equilibrium is reached in infinitesimal time, we can make the quasi-steady approximation, setting $\partial\theta/\partial t \approx 0$ in (18) to obtain

$$0 \approx \frac{1}{r^2} \frac{\partial}{\partial r} \left(r^2 \frac{\partial \theta}{\partial r} \right). \quad (23)$$

Inspection of this equation shows that solutions must take the form $\theta(r, t) = \theta_B(t)/r$. This predicts that at small Peclet number, the thermal disturbance close to the blob should scale as r^{-1} (Figure 3).

3.2. Nonlinear Melting

[35] Melting experiments on pyroxenite by *Pertermann and Hirschmann* [2003a] are best fit with $a \approx 1/4$, so we now examine solutions for that case. Since equation (14) is then nonlinear, we must rely on numerical methods to solve the

problem (see Appendix B). Figure 4 shows the results of a suite of calculations for different values of Pe , with $a = 1/4$. As with the case of $a = 1$, the curves for $F_B(t)$ are bounded above and below by asymptotes for $\text{Pe} \rightarrow 0$ and $\text{Pe} \rightarrow \infty$, respectively. The latter case, representing adiabatic melting, results in a temperature evolution given by

$$\Theta_B(t; \text{Pe} \rightarrow \infty) = \frac{1}{2\Lambda} \left(\sqrt{1 + \frac{4\Lambda t}{\Delta\theta + aS}} - 1 \right), \quad (24)$$

which can be obtained from (15) and (16) by neglecting the term describing conduction of heat into the blob. The $\text{Pe} \rightarrow 0$ case represents melting in thermal equilibrium with the surrounding mantle, and hence at the fixed temperature $\theta = 0$. Using (9a) and the definition of Θ in (10) we obtain

$$\Theta_B(t; \text{Pe} \rightarrow 0) = \frac{t}{\Delta\theta}. \quad (25)$$

Equations (24) and (25) can be substituted into the melting relationship (11); the results are plotted in Figure 4 as red, dashed lines.

[36] Figure 4b shows that the perturbation to the ambient temperature field surrounding the blob is not significantly different from the linear case. For small Peclet numbers, the temperature perturbation falls off as r^{-1} , in accordance with a quasi-steady approximation (23) of the diffusion equation.

3.3. Radially Variable Melting Within the Blob

[37] At small Peclet number, diffusion efficiently transports heat to the center of the blob, and neutralizes

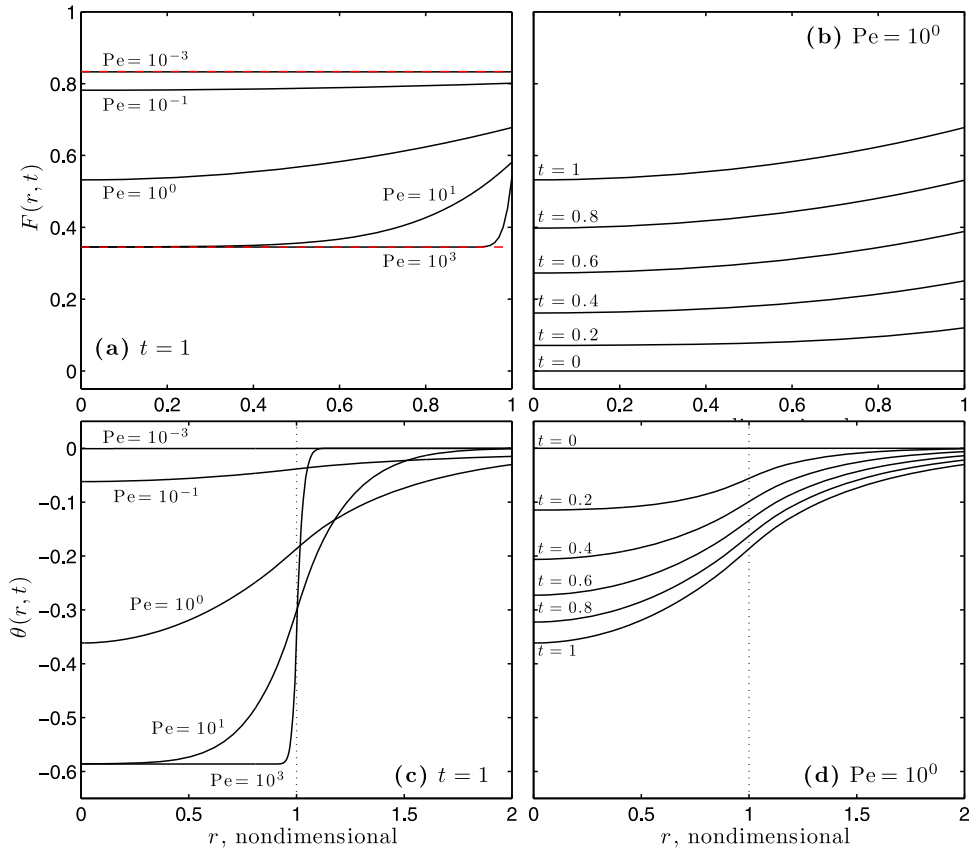


Figure 5. Radial profiles of melt fraction $F(r, t)$ and temperature $\theta(r, t)$ through the blob with $a = 1$ (compare with Figure 6 of *Sleep* [1984]). (a) $F(r, t)$ at $t = 1$ for different values of Pe . Red, dashed lines are the asymptotic values of $F(r < 1, t)$ for $Pe \rightarrow 0, \infty$. (b) $F(r, t)$ at $Pe = 1$ for different values of t . (c) $\theta(r, t)$ at $t = 1$ for different values of Pe . (d) $\theta(r, t)$ at $Pe = 1$ for different values of t .

any temperature gradients. In contrast, when the Peclet number is $\mathcal{O}(1)$, the time-scale for diffusion of heat across the blob is comparable to the time for vertical advection through the domain. In this case, we expect a significant temperature gradient across the radius of the blob, with warmer temperatures at the edge and cooler temperatures at the center. For larger Peclet numbers, diffusive heat transport is inefficient, and the temperature gradient does not penetrate far into the blob, but rather yields higher temperatures and melt fractions in a rim at the edge of the domain. To capture the behavior for $Pe \gtrsim 1$, we relax the assumption of homogeneous properties $F_B(t)$ and $\theta_B(t)$ within the blob, and instead calculate radially variable properties $F(r, t)$ and $\theta(r, t)$. This is the approach taken by *Sleep* [1984], although his calculations used 1-dimensional Cartesian rather than spherical geometry. In this section we consider only the linear melting relation, $a = 1$; based on the similarity of Figures 3 and 4, we infer that comparable behavior would be observed for the non-linear case. For $a = 1$, the Laplace transform method

can be used, with a numerical scheme to invert the transform (details and references in section A2).

[38] Figure 5 shows the results of calculations for a radially variable blob. Figure 5a illustrates the discussion in the preceding paragraph about the structure of the blob at Peclet numbers around or above unity. The degree of melting shows a radial dependence at $Pe \approx 1$ and this gradient steepens and localizes with increasing Pe . Figure 5b shows the evolution of the radially resolved degree of melting with time, for $Pe = 1$. From an early state that is nearly homogeneous in F , the diffusive heat flux penetrates progressively further into the blob with time, as shown in Figure 5d, and establishes a temperature gradient that spans the radius of the blob. Figure 5c compares the final temperature distribution within and outside the blob for a range of Peclet numbers. Section 4.1 includes a quantitative comparison of the radially resolved model and the radially averaged model, showing that

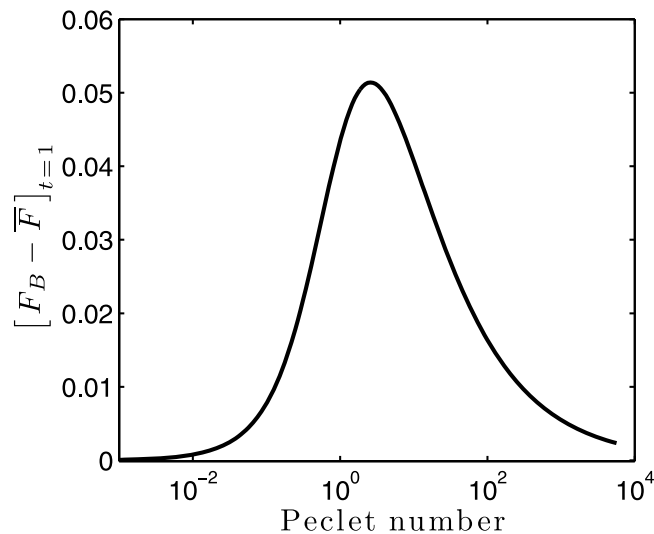


Figure 6. Difference between the radially averaged $F_B(t)$ and the radially resolved $\bar{F}(t)$ solutions for $a = 1$ at time $t = 1$. For comparison, the radially resolved solution has been averaged over the blob. The temperature difference between the two models (not shown) is a factor of $\Delta\theta$ larger than the difference in degree of melting.

differences are relatively small, but are maximized for $1 \lesssim \text{Pe} \lesssim 10$.

[39] We obtain a parallel set of results (not shown) for the case of the tabular vein, with moderate but systematic differences from those above. Part of the discussion below is a comparison of results for spherical and tabular models.

4. Discussion

[40] In this section we make a detailed examination of results for spherical and tabular heterogeneities. Before doing that, however, we compare the behavior of the radially averaged spherical model (Figures 3 and 4) with the radially resolved spherical model (Figure 5). Most of this Discussion section compares results as a function of the Peclet number, but at the end, we interpret the results in terms of dimensional heterogeneity size and upwelling rate. At that point, we also provide a quantitative comparison with the results obtained by Sleep [1984].

4.1. Model Behavior as a Function of Peclet Number

[41] Section 3.3 showed that at intermediate and large Peclet numbers, the spherical blob can have significant radial structure. What error do we make, then, in assuming a homogeneous distribution of melting *a priori*? Figure 6 shows that in terms of mean quantities, this difference is rather small (the

radially resolved model has been averaged over the spherical blob to produce an *a posteriori* mean). In general, the figure shows that the assumption of a homogeneous blob leads to a larger melt production and larger temperature contrast. This is because imposing homogeneity within the blob is equivalent to requiring that diffusion is infinitely fast there, leading to perfect redistribution of energy. Without this assumption, the rim of the sphere warms more rapidly than the core, and insulates it from inward diffusion of heat. The difference is largest at intermediate Peclet numbers because there, as shown in Figure 5, the gradient in F and θ spans much or all of the spherical blob radius.

[42] The maximum difference for the mean degree of melting between the two models is about 5%, and indicates that a blob at $\text{Pe} \approx 1$ may melt to $\sim 60\%$ rather than $\sim 65\%$ (for $a = 1$). In the present idealized context, this difference may be considered insignificant. Similar models that assume progressive removal of melt from the blob (e.g., fractional melting), or that are concerned with the chemistry of individual “packets” of melt produced within the blob, might find the assumption of homogeneity to be problematic, especially for large Peclet numbers.

[43] How does melting vary as a function of Peclet number? Figure 7 provides an answer in terms of the mean degree of melting (Figure 7a) and temperature (Figure 7b) inside the heterogeneity. Evidently, for Peclet numbers smaller than $\sim 10^{-1}$,

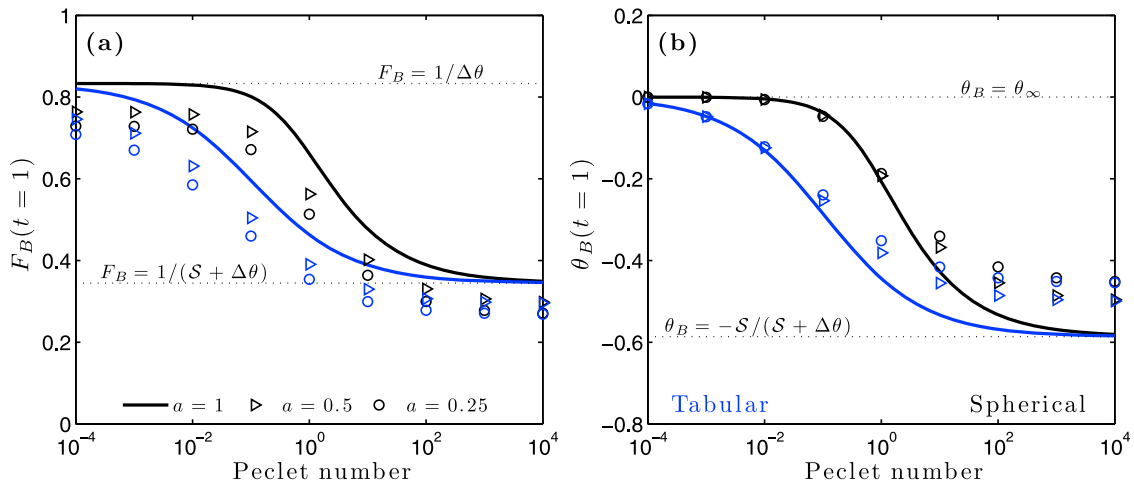


Figure 7. (a) Summary of degree of melting and (b) dimensionless temperature at $t = 1$ for three values of a , computed for a range in Peclet number spanning the transition between asymptotic values. Black lines and symbols correspond to the spherical-blob model; blue lines and symbols correspond to the tabular-vein model. Dotted lines show asymptotic values as labeled. Note that in interpreting Pe for the tabular vein, R is the half-width, as shown in Figure 1.

diffusion of heat into the spherical blob (black lines & symbols) dominates the melting budget and keeps the temperature of the blob equal to the ambient temperature. For Peclet numbers larger than $\sim 10^2$, diffusion of heat makes a negligible contribution to the overall budget and blob temperatures approach their adiabatic limit (although Figure 5a shows that the diffusive heat flux may be important in a narrow rim at the edge of the blob). In the intermediate-Peclet regime, diffusion makes a significant but not dominant contribution, and the final degree of melting and blob temperature are sensitive to the value of Pe.

[44] The tabular vein shows a qualitatively similar behavior (blue lines and symbols in Figure 7). At very large Peclet numbers, where diffusion makes an insignificant contribution to melting, the spherical blob and the tabular vein melt to equal extents; at very small Peclet numbers, where diffusion makes a substantial contribution to powering melting, the two also agree. Differences appear between these extremes, with the tabular vein exhibiting less extensive melting at any intermediate value of Pe. This can be understood in terms of the symmetry of each blob shape. In the spherical case, a circular patch on the surface of the heterogeneity draws a diffusive heat flow from a (truncated) cone of mantle, its volume increasing with the cube of distance from the blob. In the tabular case, a circular patch on the surface of the heterogeneity draws heat only from a cylinder of mantle, with a volume proportional to linear distance from the vein.

[45] Figure 7 also shows that the nonlinearity of the temperature–melting function (11) has a simple and uniform effect on the final degree of melting and the final temperature. Lower values of a require higher temperature to reach a given F_B . With other parameters held constant, decreasing a gives smaller F_B as a function of time, which means less conversion of sensible to latent heat, and therefore a smaller blob-temperature difference from ambient. Since it is this temperature difference that drives thermal diffusion and further melting, the diffusive flow of energy into the blob decreases with decreasing a .

[46] Despite reductions to maximum F_B from nonlinear effects, geometry of the heterogeneity, and adiabatic decompression (which gives a $\sim 10\%$ reduction), melting at low Peclet numbers yields degrees of partial melting that are well in excess of 50%. And while less fertile compositions than the ones considered here would generate smaller F_B , our prediction should hold if the G2 pyroxenite composition of *Pertermann and Hirschmann* [2003a] is representative of recycled oceanic crust. Furthermore, Figure 7a shows that even for the nonlinear case, we can approximate the maximum increase in degree of melting due to thermal diffusion by $1/\lambda$ where

$$\frac{1}{\lambda} = \frac{S + \Delta\theta}{\Delta\theta} = \frac{L + c_p\Delta T}{c_p\Delta T}, \quad (26)$$

which is independent of the temperature difference $\gamma/\Delta p$ between the solidii of recycled oceanic crust

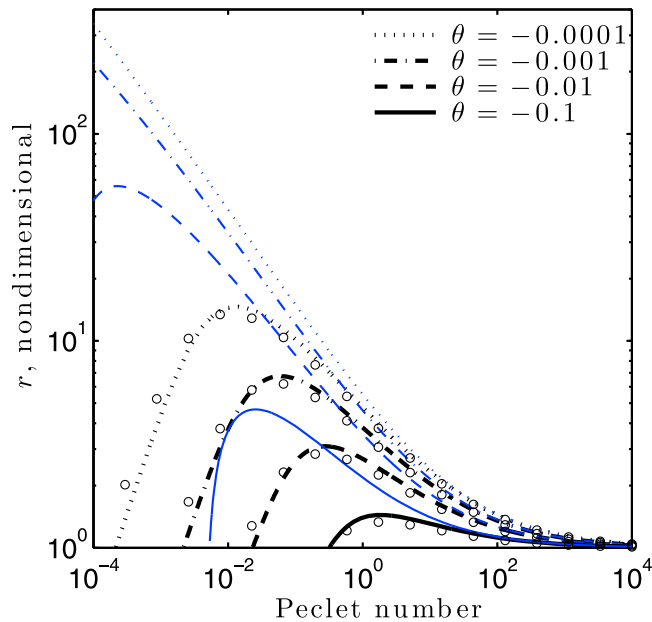


Figure 8. The non-dimensional size of the diffusively cooled halo around the spherical blob (black) and the tabular vein (blue) at $t = 1$, as a function of the Peclet number. Lines are calculated with the analytical solution for $a = 1$; each line represents the radius at which $\theta(r, 1)$ reaches a specified value (see legend for values). Points are derived from spherical-blob simulations with $a = 1/4$; their close correspondence with the lines indicates the associated value of $\theta(r, 1)$.

and depleted upper mantle (recall that L is latent heat, c_p is specific heat capacity, and ΔT is the liquidus–solidus temperature interval of pyroxenite). This equation is equivalent to equation (11) of *Sleep* [1984].

[47] How broad is the effect of melting within the heterogeneity on the mantle temperature around it? Figure 8 addresses this question for a range of Peclet numbers for both the spherical blob (black lines and symbols) and the tabular vein (blue lines). At large values of Pe , diffusion is highly localized near the heterogeneity, causing large differences from the ambient temperature in a narrow region. Moving toward smaller values of Pe , diffusion becomes more efficient, and heat flows into the heterogeneity from a broad region. In the spherical geometry, the volume of this region increases with the cube of distance from the blob; when a large volume of ambient mantle contributes heat to the blob, the ambient temperature change associated with that contribution is small. These two tendencies are reflected by the trends in Figure 8, following the black curves from right to left. At $Pe \approx 1$, where advective and diffusive heat transport are roughly in balance for the spherical heterogeneity, we find a thermal perturbation that is relatively large in both amplitude and extent. In Cartesian geometry,

volume increases linearly with distance from the tabular vein, and hence for a given inward heat flow, the thermal halo reaches greater distances.

4.2. Dependence on Dimensional Size and Upwelling Rate

[48] To conclude the discussion we reintroduce dimensional parameters and consider, independently, the effect of changing the characteristic size R and the upwelling speed W . Although these results could be deduced from earlier, dimensionless plots, they are presented in Figure 9 for clarity. To produce this figure, we have assumed values of material parameters as given in Table 1. Figure 9a shows contours of degree of melting at $t = 1$ for $a = 1$ (analytical, black lines) and $a = 1/4$ (numerical, red lines) for a spherical heterogeneity. Degree of melting is smallest at the top-right of the figure, for large blobs that upwell rapidly and melt adiabatically, and largest at the bottom-left of the figure, for small blobs that upwell slowly and melt in thermal equilibrium with their surroundings. Figure 9b shows the dimensional temperature perturbation at a distance $1.5 R$ from the center of the blob. For large blobs that upwell rapidly, loss of heat from the ambient mantle by diffusion into the blob occurs in a region narrowly confined around the

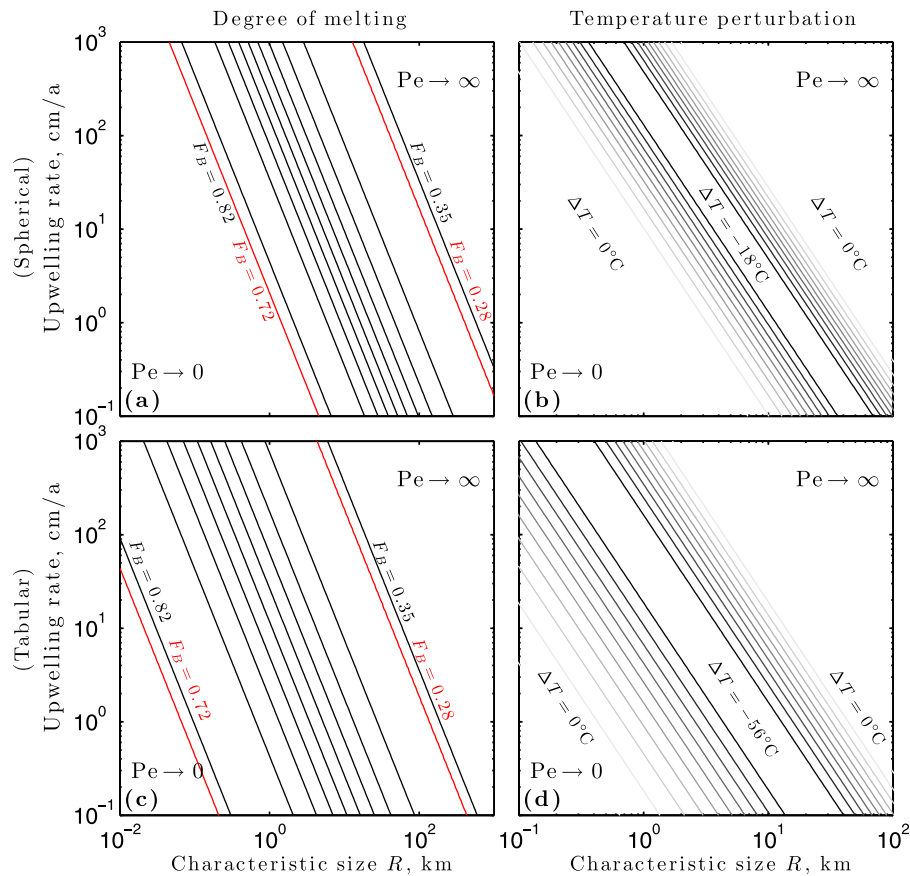


Figure 9. Contour plots of dimensional quantities as a function of characteristic heterogeneity size R in km and upwelling rate W in cm/yr. Other dimensional parameters as in Table 1. (a and c) Degree of melting for the spherical blob and tabular vein, respectively. Black contours are computed with the analytical solution and $a = 1$; red contours are computed with the numerical simulation and $a = 1/4$. Degree of melting is maximal in the bottom left corner and minimal in the top right corner. Contour spacing is linear and the maximum (minimum) contour values are 1% (more) than the appropriate asymptotic values. Asymptotic values for F_B are obtained using equations (24) and (25) with equation (11). For the nonlinear melting solution, only the maximum and minimum contours are shown. (b and d) The temperature perturbation at a distance $1.5 R$ from the center of the spherical blob or tabular vein, respectively. The largest absolute perturbation is $\sim 20^\circ\text{C}$ (spherical) and $\sim 56^\circ\text{C}$ (tabular) at this radius. Only the linear $a = 1$ solution is plotted for temperature. As in previous figures, the results here exclude the background adiabatic gradient (see A5 for details).

edge of the blob, hence the temperature at $r = 1.5 R$ is unaffected. For small blobs that upwell slowly, the heat required to maintain thermal equilibrium with the ambient mantle is small, and it is extracted over a very large volume around the blob, including $r = 1.5 R$. The case of a tabular vein is shown by contours of degree of melting and temperature perturbation in Figures 9c and 9d. The transition to diffusion-dominated melting is shifted to lower Peclet numbers, meaning that tabular veins must be narrower or upwelling more slowly to overcome their geometry and reach the same F_B as spherical blobs. Finally, note that contours in all four panels have a slope of -2 , which is consistent with the dependence of Peclet number on R and W (note different x -scales in the two panels in Figure 9).

[49] Results presented here are qualitatively consistent with those obtained by Sleep [1984]. Where his scaling analysis predicted a transition between thermally isolated and thermally equilibrated at a characteristic size of about five kilometers for an upwelling rate of 3 cm/yr, Figure 9c suggests that for a tabular vein, the transition occurs at a slightly smaller size of about one kilometer. This difference is insignificant given the model assumptions. More substantial differences can be noted in the amount of melting and the enhancement factors obtained by Sleep [1984] compared to our work. His model considered only the linearized melting relationship $a = 1$, and used an isobaric productivity of 0.02 K^{-1} corresponding to a temperature difference between the liquidus and solidus of $\Delta T = 50 \text{ K}$. This is about

a factor of five smaller than the liquidus–solidus difference obtained empirically by *Pertermann and Hirschmann* [2003a]; furthermore, near-solidus productivity for G2 pyroxenite is about 0.001 K^{-1} , a factor of 20 smaller than the value used by *Sleep* [1984]. This difference, as prescribed by equation (26), explains the very large enhancement factors ($3\text{--}7 \times$ adiabatic) that he obtained. Despite this enhancement to melting, the melt fractions reported by *Sleep* [1984] are small relative to those obtained here. This is because he computed melting curves for only 5 to 12 km of mantle ascent, which again is small relative to the value of ~ 50 km between the melting onset-depth of pyroxenite and peridotite, as estimated by *Pertermann and Hirschmann* [2003a] and used here.

5. Summary and Implications

[50] In this paper we have presented new theory for the melting of fertile mantle heterogeneities, and shown that a properly formulated Peclet number measures the importance of diffusion-driven versus adiabatic melting. Our results also show that a simplified theory that considers a uniformly melting spherical blob, rather than one that captures the gradient in F and T with radius, accurately models the gross behavior of the system, deviating only for Peclet numbers near unity. For intermediate values of upwelling rate, our model predicts that uniformly melting spherical blobs $\lesssim 5$ km in radius have substantial melt enhancement by diffusion; for tabular veins, this transition occurs at a smaller size of $\lesssim 1$ km. These conclusions confirm and extend the scaling analysis of *Sleep* [1984].

[51] Under the assumptions and parameter choices listed above, we have demonstrated that diffusion of heat into an upwelling, fertile heterogeneity can lead to an increase in the degree of partial melting by a factor of two, generating extents of melting of 50–80% beneath the bottom of the ambient melting region. Furthermore, we have shown that the thermal anomaly imprinted on the ambient mantle is confined to within about two times the characteristic size of the heterogeneity, and ranges down to about -60 K. This temperature difference is small relative to the absolute temperature of the mantle, but significant when compared with the temperature drop due to decompression melting beneath a ridge. As such, melting of the ambient mantle will be suppressed in the neighborhood of a heterogeneity, with the onset of ambient melting occurring at shallower depths. The expected change in the overall degree of ambient mantle melting due

to this effect is on the order of 1–2% for a pyroxenite fraction of 5% [*Phipps Morgan*, 2001].

[52] A detailed consideration of the geochemical implications of variable melting of heterogeneities based on their size and shape is beyond the scope of the present paper. It might be argued, for example, that larger heterogeneities, which melt to lesser extents, preserve residual garnet to shallower depth, and hence may impart a greater garnet signature than smaller heterogeneities. Such arguments are based on the details of the partition coefficients, the mineral mode of recycled oceanic crust, and the rate and style of melt segregation from pyroxenitic heterogeneities [e.g., *Prytulak and Elliott*, 2009]. Moreover, most geochemical models of the contribution of magma from recycled oceanic crust indicate that to preserve a distinctive geochemical signature, such melts must ascend rapidly, in chemical isolation from the ambient mantle. This is thought to occur either by hydrofracture and propagation of dikes, or by reactive flow and transport through high-flux dunite channels [e.g., *Kelemen et al.*, 1995; *Lundstrom et al.*, 2000; *Spiegelman and Kelemen*, 2003; *Elliott and Spiegelman*, 2003; *Kogiso et al.*, 2004].

[53] In this context, we emphasize that because the rate of reactive melting is proportional to the vertical magmatic flux, a local excess of melt supplied to the melting region from below can induce reactive channelization [*Hewitt*, 2010; *Liang et al.*, 2010]. This prediction, considered in light of the large extents of melting for recycled crust below the base of ambient-mantle melting regime, supports the hypothesis by *Lundstrom et al.* [2000] that melt released from a fertile heterogeneity could induce chemically isolated, channelized melt transport. Furthermore, it is possible that the pyroxenite-derived magmatic flux through a channel would reduce the local solidus temperature, cool the channel by consumption of latent heat, and give rise to a diffusive flux of heat into the channel (as we predict to occur around the heterogeneity). A cool diffusion-halo around a dunite channel will suppress adjacent melting of mantle peridotite, further isolating the magma as it is transported.

Appendix A: Analytical Solutions

A1. Homogeneous Melting of a Spherical Blob

[54] When the degree of melting is linearly dependent on the homologous temperature ($a = 1$



in (11)), analytical methods can be used to obtain solutions. For the homogeneous blob, the problem is to solve for $\theta(r, t)$ satisfying (18),

$$\frac{\partial \theta}{\partial t} = \frac{1}{\text{Pe}} \frac{1}{r^2} \frac{\partial}{\partial r} \left(r^2 \frac{\partial \theta}{\partial r} \right), \quad (\text{A1})$$

with boundary conditions

$$-\frac{S}{\Delta\theta} + \left(1 + \frac{S}{\Delta\theta} \right) \frac{\partial \theta}{\partial t}(1, t) = \frac{3}{\text{Pe}} \frac{\partial \theta}{\partial r}(1, t), \quad (\text{A2})$$

$$\theta(\infty, t) = 0, \quad (\text{A3})$$

and initial condition

$$\theta(r, 0) = 0. \quad (\text{A4})$$

The first of the two boundary conditions represents the heat balance between the heat flowing into the blob due to the temperature gradient outside, the heat used to melt the blob (latent heat), and the heat used to raise the temperature of the blob (sensible heat). The expression (A2) follows directly from (10), (11), and (12) when $a = 1$ (and also follows from partial differentiation with respect to t of the integral boundary condition described by (17) and (19a)). The second boundary condition states that the far-field temperature is constant (i.e., neglecting adiabatic decompression effects: see A5 for discussion of these effects). The total degree of melting of the blob can be obtained from (9a), (10), and (11) as

$$F_B(t) = \frac{\theta(1, t) + t}{\Delta\theta}. \quad (\text{A5})$$

[55] In order to simplify later algebra, it is helpful to rescale time and temperature by the Peclet number and introduce a parameter λ as

$$\theta' = \frac{\theta}{\text{Pe}}, \quad t' = \frac{t}{\text{Pe}}, \quad \lambda = \frac{\Delta\theta}{S + \Delta\theta}. \quad (\text{A6})$$

With this new scaling, the problem becomes

$$\frac{\partial \theta'}{\partial t'} = \frac{1}{r^2} \frac{\partial}{\partial r} \left(r^2 \frac{\partial \theta'}{\partial r} \right), \quad (\text{A7})$$

with boundary conditions and initial condition

$$\frac{\partial \theta'}{\partial t'}(1, t') = -1 + \lambda + 3\lambda \frac{\partial \theta'}{\partial r}(1, t'), \quad (\text{A8})$$

$$\theta'(\infty, t') = 0, \quad (\text{A9})$$

$$\theta'(r, 0) = 0, \quad (\text{A10})$$

and

$$F_B(t') = \frac{\text{Pe}}{\Delta\theta} (\theta'(1, t') + t'). \quad (\text{A11})$$

For the remainder of this appendix, we will drop the primes and use the rescaled variables.

[56] **Laplace transform solution:** The governing partial differential equation (A7) can be simplified by introducing a new variable $u(r, t)$ as

$$\theta(r, t) = \frac{u(r, t)}{r}, \quad (\text{A12})$$

to give

$$\frac{\partial u}{\partial t} = \frac{\partial^2 u}{\partial r^2} \quad (\text{A13})$$

with boundary conditions and initial condition

$$\frac{\partial u}{\partial t}(1, t) = -1 + \lambda + 3\lambda \left(\frac{\partial u}{\partial r}(1, t) - u(1, t) \right), \quad (\text{A14})$$

$$u(r, t)/r \rightarrow 0 \quad \text{as } r \rightarrow \infty, \quad (\text{A15})$$

$$u(r, 0) = 0. \quad (\text{A16})$$

[57] Introduce the Laplace transform in time as

$$\tilde{u}(r, s) = \int_0^\infty u(r, t) e^{-st} dt. \quad (\text{A17})$$

The transformed problem is then

$$s\tilde{u} = \frac{\partial^2 \tilde{u}}{\partial r^2}, \quad (\text{A18})$$

with boundary conditions

$$s\tilde{u}(1, s) = \frac{-1 + \lambda}{s} + 3\lambda \left(\frac{\partial \tilde{u}}{\partial r}(1, s) - \tilde{u}(1, s) \right), \quad (\text{A19})$$

$$\tilde{u}(r, s)/r \rightarrow 0 \quad \text{as } r \rightarrow \infty. \quad (\text{A20})$$

(A18) and (A20) imply

$$\tilde{u}(r, s) = A(s) e^{-\sqrt{s}(r-1)}, \quad (\text{A21})$$

for some function $A(s)$ to be determined. (A19) then becomes

$$sA(s) = \frac{-1 + \lambda}{s} + 3\lambda (-\sqrt{s}A(s) - A(s)) \quad (\text{A22})$$

which gives $A(s)$ as

$$A(s) = \frac{-1 + \lambda}{s(s + 3\lambda\sqrt{s} + 3\lambda)}. \quad (\text{A23})$$

Hence we have

$$\tilde{\theta}(r, s) = \frac{(\lambda - 1)e^{-\sqrt{s}(r-1)}}{rs(s + 3\lambda\sqrt{s} + 3\lambda)}. \quad (\text{A24})$$

To find $\theta(r, t)$ we need to find the inverse Laplace transform of the above function. This can be obtained by factoring the denominator, splitting into partial fractions, and performing the inverse Laplace transform term-by-term. Writing

$$\frac{1}{s(s + 3\lambda\sqrt{s} + 3\lambda)} \equiv \frac{1}{s(\sqrt{s} + a_\lambda)(\sqrt{s} + b_\lambda)} \quad (\text{A25})$$

where

$$a_\lambda = \frac{3\lambda + \sqrt{9\lambda^2 - 12\lambda}}{2}, \quad b_\lambda = \frac{3\lambda - \sqrt{9\lambda^2 - 12\lambda}}{2}, \quad (\text{A26})$$

the inverse Laplace transform of $\tilde{\theta}(r, s)$ is

$$\theta(r, t) = \frac{\lambda - 1}{r} \left[\frac{1}{a_\lambda b_\lambda} \operatorname{erfc}(\eta) + \frac{e^{-\eta^2}}{a_\lambda - b_\lambda} \cdot \left(\frac{1}{a_\lambda} w(i\eta + ia_\lambda\sqrt{t}) - \frac{1}{b_\lambda} w(i\eta + ib_\lambda\sqrt{t}) \right) \right], \quad (\text{A27})$$

where $\eta = (r - 1)/(2\sqrt{t})$ and $w(z) = e^{-z^2} \operatorname{erfc}(-iz)$ is the Faddeeva function. (A27) is the analytical solution to the linear homogeneous blob problem, and can be calculated rapidly with the aid of efficient routines for calculating the Faddeeva function [Weideman, 1994]. A solution similar to the above was recently obtained by Oliver [2008] for a related problem of spherical heat generation and conduction. The corresponding degree of melting is given by (A11),

$$F_B(t) = \frac{\text{Pe}}{\Delta\theta} \left(t + (\lambda - 1) \cdot \left[\frac{1}{a_\lambda b_\lambda} + \frac{1}{a_\lambda - b_\lambda} \left(\frac{1}{a_\lambda} w(ia_\lambda\sqrt{t}) - \frac{1}{b_\lambda} w(ib_\lambda\sqrt{t}) \right) \right] \right), \quad (\text{A28})$$

and is plotted in Figure 3.

[58] The expressions in (A27) and (A28) are somewhat cumbersome to work with when studying the asymptotic behaviors of the solution. It is easier to study the asymptotic behavior of the Laplace transform solution in s , and then relate the asymptotics in s to the asymptotics in t (see A5). For this purpose, note that $\tilde{F}_B(s)$ is given by the expression

$$\tilde{F}_B(s) = \frac{\text{Pe}}{\Delta\theta} \left(\frac{1}{s^2} + \tilde{\theta}(1, s) \right) = \frac{\text{Pe}}{\Delta\theta} \left(\frac{1}{s^2} + A(s) \right). \quad (\text{A29})$$

A2. Radially Variable Melting of a Spherical Blob

[59] If we do not assume that the blob is homogeneous, and instead allow it to have a radial temperature profile due to the conduction of heat through the blob, then we must solve the heat conservation equation both inside and outside the blob. Using the rescaled variables of (A26), the governing equations are

$$\frac{\partial\theta}{\partial t} = -1 + \lambda + \frac{\lambda}{r^2} \frac{\partial}{\partial r} \left(r^2 \frac{\partial\theta}{\partial r} \right), \quad 0 \leq r < 1, \quad (\text{A30})$$

$$\frac{\partial\theta}{\partial t} = \frac{1}{r^2} \frac{\partial}{\partial r} \left(r^2 \frac{\partial\theta}{\partial r} \right), \quad r > 1. \quad (\text{A31})$$

On the surface of the blob, both the temperature and the heat flux must be continuous, i.e.,

$$\theta(r, t), \frac{\partial\theta}{\partial r}(r, t) \text{ continuous on } r = 1, \quad (\text{A32})$$

and as before the initial condition is

$$\theta(r, 0) = 0, \quad (\text{A33})$$

and the boundary condition in the far-field is

$$\theta(\infty, t) = 0. \quad (\text{A34})$$

[60] **Laplace transform solution:** As before, the governing partial differential equations can be simplified by writing

$$\theta(r, t) = \frac{u(r, t)}{r} \quad (\text{A35})$$

to obtain

$$\frac{\partial u}{\partial t} = (\lambda - 1)r + \lambda \frac{\partial^2 u}{\partial r^2}, \quad 0 \leq r < 1, \quad (\text{A36})$$

$$\frac{\partial u}{\partial t} = \frac{\partial^2 u}{\partial r^2}, \quad r > 1, \quad (\text{A37})$$

with boundary and initial conditions

$$u(r, t), \frac{\partial u}{\partial r}(r, t) \text{ continuous on } r = 1, \quad (\text{A38})$$

$$u(r, t)/r \text{ finite as } r \rightarrow 0, \quad (\text{A39})$$

$$u(r, t)/r \rightarrow 0 \text{ as } r \rightarrow \infty, \quad (\text{A40})$$

$$u(r, 0) = 0. \quad (\text{A41})$$

[61] The Laplace transformed problem is

$$s\tilde{u} = \frac{(\lambda - 1)r}{s} + \lambda \frac{\partial^2 \tilde{u}}{\partial r^2}, \quad 0 \leq r < 1, \quad (\text{A42})$$

$$s\tilde{u} = \frac{\partial^2 \tilde{u}}{\partial r^2}, \quad r > 1, \quad (\text{A43})$$

with boundary conditions

$$\tilde{u}(r, s), \frac{\partial \tilde{u}}{\partial r}(r, s) \text{ continuous on } r = 1, \quad (\text{A44})$$

$$\tilde{u}(r, s)/r \text{ finite as } r \rightarrow 0, \quad (\text{A45})$$

$$\tilde{u}(r, s)/r \rightarrow 0 \text{ as } r \rightarrow \infty. \quad (\text{A46})$$

The governing equations (A42) and (A43) can be integrated using the boundary conditions (A45) and (A46) to give

$$\tilde{u}(r, s) = \begin{cases} \frac{(\lambda - 1)r}{s^2} + B(s) \sinh\left(\sqrt{\frac{s}{\lambda}} r\right), & 0 \leq r < 1, \\ C(s)e^{-\sqrt{s}(r-1)}, & r > 1. \end{cases} \quad (\text{A47})$$

The two functions $B(s)$ and $C(s)$ are determined by the continuity requirements of (A44)

$$B(s) = -\frac{\lambda - 1}{s^2} \left(\frac{1 + \sqrt{s}}{\sqrt{\frac{s}{\lambda}} \cosh \sqrt{\frac{s}{\lambda}} + \sqrt{s} \sinh \sqrt{\frac{s}{\lambda}}} \right), \quad (\text{A48})$$

$$C(s) = \frac{\lambda - 1}{s^2} \left(\frac{\sqrt{\frac{s}{\lambda}} \cosh \sqrt{\frac{s}{\lambda}} - \sinh \sqrt{\frac{s}{\lambda}}}{\sqrt{\frac{s}{\lambda}} \cosh \sqrt{\frac{s}{\lambda}} + \sqrt{s} \sinh \sqrt{\frac{s}{\lambda}}} \right). \quad (\text{A49})$$

The solution for $\tilde{\theta}(r, s)$ is thus

$$\tilde{\theta}(r, s) = \begin{cases} \frac{(\lambda - 1)}{s^2} + \frac{B(s)}{r} \sinh\left(\sqrt{\frac{s}{\lambda}} r\right), & 0 \leq r < 1, \\ \frac{C(s)}{r} e^{-\sqrt{s}(r-1)}, & r > 1. \end{cases} \quad (\text{A50})$$

To find $\theta(r, t)$ we must obtain the inverse Laplace transform of the above function. Unfortunately, there does not appear to be a simple analytical inverse of (A50). However, the inverse can be calculated numerically using efficient routines for numerical inverse Laplace transforms [de Hoog *et al.*, 1982; K. Hollenbeck, INVLAP.M: A matlab function for numerical inversion of Laplace transforms by the de Hoog algorithm, 1998, <http://www.isva.dtu.dk/staff/karl/invlap.htm>, hereinafter referred to as Hollenbeck, matlab function, 1998].

[62] The degree of melting within the blob is given by

$$F(r, t) = \frac{\text{Pe}}{\Delta\theta} (t + \theta(r, t)), \quad (\text{A51})$$

and hence using (A50) we have

$$\tilde{F}(r, s) = \frac{\text{Pe}}{\Delta\theta} \left(\frac{1}{s^2} + \tilde{\theta}(r, s) \right) = \frac{\text{Pe}}{\Delta\theta} \left(\frac{\lambda}{s^2} + \frac{B(s)}{r} \sinh \sqrt{\frac{s}{\lambda}} r \right). \quad (\text{A52})$$

The Laplace transform of the mean degree of melting $\bar{F}(t)$ is thus

$$\begin{aligned} \bar{\tilde{F}}(s) &= 3 \int_0^1 \tilde{F}(r, s) r^2 dr \\ &= \frac{\text{Pe}}{\Delta\theta} \left(\frac{\lambda}{s^2} + \frac{3B(s)\lambda}{s} \left(\sqrt{\frac{s}{\lambda}} \cosh \sqrt{\frac{s}{\lambda}} - \sinh \sqrt{\frac{s}{\lambda}} \right) \right) \\ &= \frac{\text{Pe}\lambda}{\Delta\theta} \left(\frac{1}{s^2} - \frac{3}{s} (1 + \sqrt{s}) C(s) \right). \end{aligned} \quad (\text{A53})$$

$\bar{F}(t)$ can be obtained by finding the inverse Laplace transform of the above function. This was done numerically using the routines of Hollenbeck (matlab function, 1998) to produce the profiles plotted in Figure 5.

A3. Melting of a Tabular Vein

[63] In this section we briefly derive the tabular equivalents of the solutions given in A1 and A2. The general method of solution for a tabular geometry is identical to that for a spherical geometry. The only change that needs to be made is that the Laplacian operator is now given by

$$\nabla^2 = \frac{\partial^2}{\partial x^2} \quad (\text{A54})$$

where $0 < x < 1$ is inside the sheet, and $x > 1$ is outside to sheet. Symmetry is assumed about the origin, so that

$$\frac{\partial \theta}{\partial x} = 0 \quad \text{on } x = 0. \quad (\text{A55})$$

A3.1. Homogeneous Melting

[64] The problem is

$$\frac{\partial \theta}{\partial t} = \frac{\partial^2 \theta}{\partial x^2} \quad (\text{A56})$$

with boundary conditions and initial condition

$$\frac{\partial \theta}{\partial t}(1, t) = -1 + \lambda + \lambda \frac{\partial \theta}{\partial x}(1, t), \quad (\text{A57})$$

$$\theta(\infty, t) = 0, \quad (\text{A58})$$

$$\theta(x, 0) = 0. \quad (\text{A59})$$



The Laplace transformed problem is

$$s\tilde{\theta} = \frac{\partial^2 \tilde{\theta}}{\partial x^2}, \quad (\text{A60})$$

with boundary conditions

$$s\tilde{\theta}(1, s) = \frac{-1 + \lambda}{s} + \lambda \frac{\partial \tilde{\theta}}{\partial x}(1, s), \quad (\text{A61})$$

$$\tilde{\theta}(\infty, t) = 0, \quad (\text{A62})$$

and solution

$$\tilde{\theta}(x, s) = \frac{(\lambda - 1)e^{-\sqrt{s}(x-1)}}{s^{3/2}(\sqrt{s} + \lambda)}. \quad (\text{A63})$$

The inverse Laplace transform of this is

$$\theta(x, t) = \frac{\lambda - 1}{\lambda^2} \left[e^{-\eta^2} \left(w(i\eta + i\lambda\sqrt{t}) + \frac{2\lambda\sqrt{t}}{\sqrt{\pi}} \right) - (1 + 2\lambda\sqrt{t}\eta) \operatorname{erfc}(\eta) \right], \quad (\text{A64})$$

where $\eta = (x - 1)/(2\sqrt{t})$ and $w(z)$ is the Faddeeva function. The above solution can also be found in the study by *Carslaw and Jaeger* [1959] (their equation (12) in section 12.4). The corresponding degree of melting is given by

$$F_B(t) = \frac{\text{Pe}}{\Delta\theta} \left(t + \frac{\lambda - 1}{\lambda^2} \left[w(i\lambda\sqrt{t}) + \frac{2\lambda\sqrt{t}}{\sqrt{\pi}} - 1 \right] \right). \quad (\text{A65})$$

A3.2. Laterally Variable Melting

[65] The governing equations are

$$\frac{\partial \theta}{\partial t} = -1 + \lambda + \frac{\partial^2 \theta}{\partial x^2}, \quad 0 \leq x < 1, \quad (\text{A66})$$

$$\frac{\partial \theta}{\partial t} = \frac{\partial^2 \theta}{\partial x^2}, \quad x > 1. \quad (\text{A67})$$

The Laplace transformed problem is

$$s\tilde{\theta} = \frac{\lambda - 1}{s} + \lambda \frac{\partial^2 \tilde{\theta}}{\partial x^2}, \quad 0 \leq x < 1, \quad (\text{A68})$$

$$s\tilde{\theta} = \frac{\partial^2 \tilde{\theta}}{\partial x^2}, \quad x > 1. \quad (\text{A69})$$

with solution

$$\tilde{\theta}(x, s) = \begin{cases} \frac{\lambda - 1}{s^2} + B(s) \cosh\left(\sqrt{\frac{s}{\lambda}}x\right), & 0 \leq x < 1, \\ C(s)e^{-\sqrt{s}(x-1)}, & x > 1. \end{cases} \quad (\text{A70})$$

The two functions $B(s)$ and $C(s)$ are determined by continuity as

$$B(s) = -\frac{\lambda - 1}{s^2} \left(\frac{1}{\cosh \sqrt{\frac{s}{\lambda}} + \frac{1}{\sqrt{\lambda}} \sinh \sqrt{\frac{s}{\lambda}}} \right), \quad (\text{A71})$$

$$C(s) = \frac{\lambda - 1}{s^2} \left(\frac{\frac{1}{\sqrt{\lambda}} \sinh \sqrt{\frac{s}{\lambda}}}{\cosh \sqrt{\frac{s}{\lambda}} + \frac{1}{\sqrt{\lambda}} \sinh \sqrt{\frac{s}{\lambda}}} \right). \quad (\text{A72})$$

The Laplace transform of the mean degree of melting $\bar{F}(t)$ is

$$\begin{aligned} \bar{\bar{F}}(s) &= \int_0^1 \bar{F}(x, s) dx \\ &= \frac{\text{Pe}}{\Delta\theta} \left(\frac{\lambda}{s^2} + B(s) \sqrt{\frac{\lambda}{s}} \sinh \sqrt{\frac{s}{\lambda}} \right) \\ &= \frac{\text{Pe}\lambda}{\Delta\theta} \left(\frac{1}{s^2} - \frac{C(s)}{\sqrt{s}} \right). \end{aligned} \quad (\text{A73})$$

A4. Leading Order Asymptotics

[66] All the problems considered in this paper (both spherical/tabular and homogeneous/radially varying) have the same leading order behavior for large and small t . This behavior is exactly that which is expected from a simple thermodynamic analysis of the two extremes of a thermally isolated blob and a blob in thermal equilibrium with the ambient mantle. This leading order behavior has been described by *Sleep* [1984] and is depicted in Figure 2.

[67] The large- t and small- t asymptotic behavior of $F_B(t)$ and $\bar{F}(t)$ can be obtained directly from the asymptotic behavior of the Laplace transforms $\bar{F}_B(s)$ and $\bar{F}(s)$ for small s and large s respectively. The leading order asymptotics of $\bar{F}_B(s)$ are given by series expansion of (A29) as

$$\bar{F}_B(s) \sim \begin{cases} \frac{\text{Pe}\lambda}{\Delta\theta s^2} + \mathcal{O}\left(\frac{1}{s^{5/2}}\right), & \text{for } s \gg 1, \\ \frac{\text{Pe}}{\Delta\theta s} + \mathcal{O}\left(\frac{1}{s}\right), & \text{for } s \ll 1. \end{cases} \quad (\text{A74})$$

The leading order asymptotics of $\bar{F}(s)$ from (A53) are identical. By inverse Laplace transforming term-by-term we obtain the leading order asymptotics of $F_B(t)$ as

$$F_B(t) \sim \begin{cases} \frac{\text{Pe}\lambda}{\Delta\theta} t + \mathcal{O}(t^{3/2}), & \text{for } t \ll 1, \\ \frac{\text{Pe}}{\Delta\theta} + \mathcal{O}(1), & \text{for } t \gg 1. \end{cases} \quad (\text{A75})$$



The above expression can be written in dimensional units using (2) as

$$F_B(t) \sim \begin{cases} \frac{p_0 - p(t)}{\gamma(\Delta T + L/c_p)} + \mathcal{O}(t^{3/2}), & \text{for } t \ll R^2/\kappa, \\ \frac{p_0 - p(t)}{\gamma\Delta T} + \mathcal{O}(1), & \text{for } t \gg R^2/\kappa, \end{cases} \quad (\text{A76})$$

which agrees with the simple thermodynamic analysis of *Sleep* [1984] (his equations 9 and 10 respectively, see Figure 2). Higher order asymptotic expansions for $F_B(t)$ can be obtained by considering higher order terms in the series expansions of (A74). Differences between $F_B(t)$ and $\bar{F}(t)$, and the tabular and spherical geometries, become evident with the inclusion of higher order terms.

A5. Adiabatic Decompression Effects

[68] Up to this point the effects of adiabatic decompression have been ignored, as it has been assumed that the far-field temperature of the ambient mantle is constant. In fact, the far-field temperature of the ambient mantle will decrease as the pressure decreases as a consequence of adiabatic decompression. It is straightforward to include this effect, at least in a linearized sense. If the temperature differences are small, such that $(T_0 - T_1)/T_0 \ll 1$, the adiabatic decompression term in the energy equation (5) can be approximated as

$$-\alpha T \frac{\partial p}{\partial t} \approx -\alpha T_0 \frac{\partial p}{\partial t}. \quad (\text{A77})$$

The non-dimensional radially varying blob problem is then

$$\frac{\partial \theta}{\partial t} = -\lambda \mathcal{A} - 1 + \lambda + \frac{\lambda}{r^2} \frac{\partial}{\partial r} \left(r^2 \frac{\partial \theta}{\partial r} \right), \quad 0 \leq r < 1, \quad (\text{A78})$$

$$\frac{\partial \theta}{\partial t} = -\mathcal{A} + \frac{1}{r^2} \frac{\partial}{\partial r} \left(r^2 \frac{\partial \theta}{\partial r} \right), \quad r > 1, \quad (\text{A79})$$

where \mathcal{A} is the adiabatic parameter, defined by

$$\mathcal{A} = \frac{\alpha T_0 \gamma}{\rho c_p}. \quad (\text{A80})$$

The boundary conditions on the surface of the blob, and the initial condition are as before. The far-field boundary condition becomes

$$\theta(\infty, t) = -\mathcal{A}t, \quad (\text{A81})$$

reflecting the fact that the far-field temperature drops as the blob ascends. By writing

$$\theta(r, t) = -\mathcal{A}t + (1 - \mathcal{A})\vartheta(r, t), \quad (\text{A82})$$

we recover the problem that has already been solved neglecting adiabatic decompression, i.e.,

$$\frac{\partial \vartheta}{\partial t} = -1 + \lambda + \frac{\lambda}{r^2} \frac{\partial}{\partial r} \left(r^2 \frac{\partial \vartheta}{\partial r} \right), \quad 0 \leq r < 1, \quad (\text{A83})$$

$$\frac{\partial \vartheta}{\partial t} = \frac{1}{r^2} \frac{\partial}{\partial r} \left(r^2 \frac{\partial \vartheta}{\partial r} \right), \quad r > 1, \quad (\text{A84})$$

$$\vartheta(\infty, t) = 0. \quad (\text{A85})$$

Hence to calculate the solution for a problem which includes the adiabatic decompression term, we simply find the solution without the term, and then use (A82). This works for both the homogeneous and the radially varying blob problems, as well as for the tabular geometry. Since

$$F(r, t) = \frac{\text{Pe}}{\Delta \theta} (t + \theta(r, t)) = \frac{\text{Pe}}{\Delta \theta} (1 - \mathcal{A})(t + \vartheta(r, t)), \quad (\text{A86})$$

the melt productivity decreases by a factor of $(1 - \mathcal{A})$ when the adiabatic decompression term is included. For example, the values of the dimensional degree of melting at the two extremes changes from that given by (A76) to

$$F_B(t) \sim \begin{cases} \frac{p_0 - p(t)}{\Delta T + L/c_p} \left(\frac{1}{\gamma} - \frac{\alpha T_0}{\rho c_p} \right) + \mathcal{O}(t^{3/2}), & \text{for } t \ll R^2/\kappa, \\ \frac{p_0 - p(t)}{\Delta T} \left(\frac{1}{\gamma} - \frac{\alpha T_0}{\rho c_p} \right) + \mathcal{O}(1), & \text{for } t \gg R^2/\kappa. \end{cases} \quad (\text{A87})$$

The first of the above two cases can be recognized as following directly from the usual expression for the productivity during isentropic decompression melting [e.g., *Asimow et al.*, 1997, equation (3.14)]. The second case is in agreement with expressions for the productivity assuming complete thermal equilibration [e.g., *Phipps Morgan*, 2001, equation (19)].

Appendix B: Numerical Solutions

[69] The governing equations with $a < 1$ are nonlinear and must be solved numerically. To do so we use a semi-implicit, centered-difference discretization on a non-uniform grid. We solve the resulting system of nonlinear algebraic equations with a Newton-Krylov (GMRES) scheme and an explicit LU preconditioner; these are provided by the Portable, Extensible Toolkit for Scientific

Computation (version 3.1 [Balay *et al.*, 2010; Katz *et al.*, 2007; S. Balay *et al.*, PETSc Web page, 2011, <http://www.mcs.anl.gov/petsc>]). Details of the discretization are given in this appendix for the case of a spherical heterogeneity; corresponding equations for the tabular vein are obtained in a similar manner. Simulation code is available by email request to the first author.

[70] The discretization is semi-implicit in time,

$$\frac{\theta^{n+1} - \theta^n}{\Delta t} = \frac{1}{2\text{Pe}} \left[\left(\frac{1}{r^2} \frac{\partial}{\partial r} \left(r^2 \frac{\partial \theta}{\partial r} \right) \right)^{n+1} + \left(\frac{1}{r^2} \frac{\partial}{\partial r} \left(r^2 \frac{\partial \theta}{\partial r} \right) \right)^n \right], \quad (\text{B1})$$

where Δt is the time step, chosen such that $t_n = n\Delta t$ for $n \in [0, N_t - 1]$. Superscripts in the semi-discrete equation (B1) refer to the time step number.

[71] Spatial derivatives are discretized with a centered difference scheme,

$$\frac{1}{r^2} \frac{\partial}{\partial r} \left(r^2 \frac{\partial \theta}{\partial r} \right) \approx \frac{\left[\frac{(r_{i+1}+r_i)^2}{2} \left(\frac{\theta_{i+1}-\theta_i}{r_{i+1}-r_i} \right) \right] - \left[\frac{(r_i+r_{i-1})^2}{2} \left(\frac{\theta_i-\theta_{i-1}}{r_i-r_{i-1}} \right) \right]}{\frac{1}{2}(r_{i+1}-r_{i-1}) r_i^2}. \quad (\text{B2})$$

Values of the radius are specified at a set of discrete points $i \in [0, N_r - 1]$ using

$$r_i = 1 + (r_{\max} - 1) \left(\frac{i}{N_r - 1} \right)^\xi, \quad (\text{B3})$$

where $\xi \geq 1$ is a power that determines the relative concentration of grid points near the blob. We have found that $\xi = 2$ provides a good balance between accuracy and speed of numerical convergence.

[72] The boundary condition at $r \rightarrow \infty$ is a straightforward Dirichlet condition, which we apply at $r = r_{\max} \gg 1$. The boundary condition at $r = 1$ is more difficult. For $F_B \leq 1$, the semi-implicit discretization of this condition is as follows

$$\theta_0^n = -n\Delta t + \Delta\theta \Theta_B^n, \quad (\text{B4})$$

where Θ_B^n is the dimensionless homologous temperature of the blob at the present step, obtained with equation (15), which depends on the unknown value of f_B . The current Newton iterate \check{f}_B can be calculated using the current Newton iterate of the solution vector $\check{\theta}_i^n$ by discrete integration with the trapezoidal rule,

$$\check{f}_B^n = f_B^{n-1} + \frac{\Delta t}{\Delta\theta + aS} \left(1 + \frac{3}{\text{Pe}} \frac{\check{\theta}_1^n + \theta_1^{n-1} - \check{\theta}_0^n - \theta_0^{n-1}}{2(r_1 - r_0)} \right). \quad (\text{B5})$$

[73] The discrete boundary conditions and diffusion equation are then recast as equations for the elements of the point-wise Newton residual vector of the current iterate $\check{\theta}_i$. We provide an analytical Jacobian matrix $J_{ij} = \partial \check{\theta}_i / \partial \theta_j$, and the Newton scheme is iterated until the residual vector satisfies $\|\check{\theta}_i\|_2 < \text{tol}$. We use a tolerance of 10^{-10} .

[74] Numerical solutions can be compared with the analytical solution for the linear case, $a = 1$. Percent error is computed as

$$e = \frac{\|\theta_{\text{exact}} - \theta_{\text{numerical}}\|_2}{\|\theta_{\text{exact}}\|_2} \times 100, \quad (\text{B6})$$

where the 2-norm is calculated over all combinations of r_i, t_n used in the numerical model-run. We obtain perfect second order convergence with grid-spacing for grids up to $N_r = 3200$ with $\xi = 2$; we obtain little improvement in accuracy for $N_r \gtrsim 800$. For a grid with $N_r = 1600$ and $N_t = 1000$ we find that $e = 0.003\%$.

Acknowledgments

[75] The authors thank C. Langmuir and M. Hirschmann for advice and comments on the manuscript, T. Becker for his editorial efficiency, and S. Weatherley for discussions regarding melt transport. Katz was supported by a Research Councils UK Academic Fellowship and NERC grant NE/H00081X/1.

References

- Allègre, C. J., and D. L. Turcotte (1986), Implications of a two-component marble-cake mantle, *Nature*, 323(6084), 123–127.
- Asimow, P., M. Hirschmann, and E. Stolper (1997), An analysis of variations in isentropic melt productivity, *Philos. Trans. Roy. Soc. London A*, 355(1723), 255–281.
- Balay, S., J. Brown, K. Buschelman, V. Eijkhout, W. D. Gropp, D. Kaushik, M. G. Knepley, L. C. McInnes, B. F. Smith, and H. Zhang (2010), PETSc users manual, *Technical Report ANL-95/11*, revision 3.1, Argonne Natl. Lab., Argonne, Ill.
- Carslaw, H., and J. Jaeger (1959), *Conduction of Heat in Solids*, Oxford Sci. Publ., Clarendon, Oxford, U. K.
- de Hoog, F., J. Knight, and A. Stokes (1982), An improved method for numerical inversion of Laplace transforms, *SIAM J. Sci. Stat. Comput.*, 3, 357–366.
- Elliott, T., and M. Spiegelman (2003), Melt migration in oceanic crustal production: A U-series perspective, in *Treatise on Geochemistry*, vol. 3, *The Crust*, edited by R. L. Rudnick, chap. 14, pp. 465–510, Elsevier, Amsterdam.
- Gurnis, M. (1986), Quantitative bounds on the size spectrum of isotopic heterogeneity within the mantle, *Nature*, 323(6086), 317–320.
- Helfrich, G. (2006), Heterogeneity in the mantle—Its creation, evolution and destruction, *Tectonophysics*, 416(1–4), 23–31, doi:10.1016/j.tecto.2005.11.012.



- Hewitt, I. J. (2010), Modelling melting rates in upwelling mantle, *Earth Planet. Sci. Lett.*, *300*, 264–274, doi:10.1016/j.epsl.2010.10.010.
- Hirschmann, M. M., and E. M. Stolper (1996), A possible role for garnet pyroxenite in the origin of the “garnet signature” in MORB, *Contrib. Mineral. Petrol.*, *124*(2), 185–208.
- Hirschmann, M. M., P. Asimow, M. Ghiorso, and E. M. Stolper (1999), Calculation of peridotite partial melting from thermodynamic models of minerals and melts. III. Controls on isobaric melt production and the effect of water on melt production. *J. Petrol.*, *40*, 831–851.
- Hoffman, N. R. A., and D. McKenzie (1985), The destruction of geochemical heterogeneities by differential fluid motions during mantle convection, *Geophys. J. R. Astron. Soc.*, *82*, 163–206, doi:10.1111/j.1365-246X.1985.tb05134.x.
- Hofmann, A. (1997), Mantle geochemistry: The message from oceanic volcanism, *Nature*, *385*(6613), 219.
- Hofmann, A., and S. Hart (1978), An assessment of local and regional isotopic equilibrium in the mantle, *Earth Planet. Sci. Lett.*, *38*, 44–62.
- Hofmann, A., and W. White (1982), Mantle plumes from ancient oceanic crust, *Earth Planet. Sci. Lett.*, *57*(2), 421–436, doi:10.1016/0012-821X(82)90161-3.
- Ito, G., and J. Mahoney (2005), Flow and melting of a heterogeneous mantle: 2. Implications for a chemically nonlayered mantle, *Earth Planet. Sci. Lett.*, *230*(1–2), 47–63, doi:10.1016/j.epsl.2004.10.034.
- Katz, R., M. Knepley, B. Smith, M. Spiegelman, and E. Coon (2007), Numerical simulation of geodynamic processes with the Portable Extensible Toolkit for Scientific Computation, *Phys. Earth Planet. Int.*, *163*, 52–68, doi:10.1016/j.pepi.2007.04.016.
- Kelemen, P., N. Shimizu, and V. Salters (1995), Extraction of mid-ocean-ridge basalt from the upwelling mantle by focused flow of melt in dunite channels, *Nature*, *375*(6534), 747–753.
- Kogiso, T., M. Hirschmann, and P. Reiners (2004), Length scales of mantle heterogeneities and their relationship to ocean island basalt geochemistry, *Geochim. Cosmochim. Acta*, *68*(2), 345–360.
- Liang, Y., A. Schiemenz, M. A. Hesse, E. M. Parmentier, and J. S. Hesthaven (2010), High-porosity channels for melt migration in the mantle: Top is the dunite and bottom is the harzburgite and lherzolite, *Geophys. Res. Lett.*, *37*, L15306, doi:10.1029/2010GL044162.
- Liang, Y., A. Schiemenz, M. Hesse, and E. Parmentier (2011), Waves, channels, and the preservation of chemical heterogeneities during melt migration in the mantle, *Geophys. Res. Lett.*, doi:10.1029/2011GL049034, in press.
- Lundstrom, C., J. Gill, and Q. Williams (2000), A geochemically consistent hypothesis for MORB generation, *Chem. Geol.*, *162*(2), 105–126.
- Oliver, D. (2008), Analytical solution for heat conduction near an encapsulated sphere with heat generation, *J. Heat Transfer*, *130*, 024502.
- Pertermann, M., and M. Hirschmann (2003a), Partial melting experiments on a MORB-like pyroxenite between 2 and 3 GPa: Constraints on the presence of pyroxenite in basalt source regions from solidus location and melting rate, *J. Geophys. Res.*, *108*(B2), 2125, doi:10.1029/2000JB000118.
- Pertermann, M., and M. Hirschmann (2003b), Anhydrous partial melting experiments on MORB-like eclogite: Phase relations, phase compositions and mineral-melt partitioning of major elements at 2–3 GPa, *J. Petrol.*, *44*(12), 2173–2201.
- Pertermann, M., M. Hirschmann, K. Hametner, D. Gunther, and M. Schmidt (2004), Experimental determination of trace element partitioning between garnet and silica-rich liquid during anhydrous partial melting of MORB-like eclogite, *Geochim. Geophys. Geosyst.*, *5*, Q05A01, doi:10.1029/2003GC000638.
- Phipps Morgan, J. (2001), Thermodynamics of pressure release melting of a veined plum pudding mantle, *Geochim. Geophys. Geosyst.*, *2*(4), 1001, doi:10.1029/2000GC000049.
- Prytulak, J., and T. Elliott (2009), Determining melt productivity of mantle sources from ²³⁸U–²³⁰Th and ²³⁵U–²³¹Pa disequilibria; an example from Pico Island, Azores, *Geochim. Cosmochim. Acta*, *73*(7), 2103–2122, doi:10.1016/j.gca.2009.01.001.
- Riley, G., and D. Kohlstedt (1991), Kinetics of melt migration in upper mantle-type rocks, *Earth Planet. Sci. Lett.*, *105*, 500–521.
- Sleep, N. (1984), Tapping of magmas from ubiquitous mantle heterogeneities, *J. Geophys. Res.*, *89*(B12), 10,029–10,041, doi:10.1029/JB089iB12p10029.
- Sobolev, A., et al. (2007), The amount of recycled crust in sources of mantle-derived melts, *Science*, *316*(5823), 412–417, doi:10.1126/science.1138113.
- Spiegelman, M. (1993), Flow in deformable porous media. part 2. Numerical analysis—The relationship between shock waves and solitary waves, *J. Fluid Mech.*, *247*, 39–63.
- Spiegelman, M., and P. Kelemen (2003), Extreme chemical variability as a consequence of channelized melt transport, *Geochim. Geophys. Geosyst.*, *4*(7), 1055, doi:10.1029/2002GC000336.
- Stolper, E., and P. Asimow (2007), Insights into mantle melting from graphical analysis of one-component systems, *Am. J. Sci.*, *307*(8), 1051–1139, doi:10.2475/08.2007.01.
- Stracke, A., V. J. M. Salters, and K. W. W. Sims (1999), Assessing the presence of garnet-pyroxenite in the mantle sources of basalts through combined hafnium-neodymium-thorium isotope systematics, *Geochim. Geophys. Geosyst.*, *1*(12), 1006, doi:10.1029/1999GC000013.
- Weideman, J. (1994), Computation of the Complex Error Function, *SIAM J. Numer. Anal.*, *31*, 1497–1518.
- Willbold, M., and A. Stracke (2010), Formation of enriched mantle components by recycling of upper and lower continental crust, *Chem. Geol.*, *276*, 188–197, doi:10.1016/j.chemgeo.2010.06.005.
- Yasuda, A., and T. Fujii (1998), Ascending subducted oceanic crust entrained within mantle plumes, *Geophys. Res. Lett.*, *25*(10), 1561–1564.
- Yaxley, G., and D. Green (1998), Reactions between eclogite and peridotite: Mantle refertilisation by subduction of oceanic crust, *Schweiz. Mineral. Petrogr. Mitt.*, *78*, 243–255.